UNIVERSITÀ DEGLI STUDI DI PADOVA

Dipartimento di Fisica e Astronomia Galileo Galilei

Corso di Laurea Magistrale in Fisica

Wavefront curvature sensing and control in microscopy

Relatore: Prof. Stefano Bonora
Relatore interno: Prof. Michele Merano

Laureando: Gianluca Dalle Rive
Matricola: 1065542

Anno Accademico 2015/2016
13 aprile 2016

To my family

Contents

Introduction **9**

1 Aberrations and adaptive optics **11**

1.1 Optical image formation 12

1.2 Zernike polynomials 12

1.3 Lukosz polynomials 14

1.4 Maréchal criterion 16

1.5 Wavefront sensors 17

1.5.1 Shack-Hartmann WFS 17

1.5.2 Curvature WFS 17

1.5.3 Pyramid WFS 18

1.5.4 Phase diversity WFS 18

1.6 Wavefront correctors: Deformable Mirrors 20

1.6.1 Segmented DMs 21

1.6.2 Continuous faceplate DMs 21

1.6.3 Membrane DMs 22

1.6.4 Bimorph DMs 23

1.6.5 Microelectromechanical DMs 23

1.7 Wavefront correctors: Deformable Lenses 23

1.7.1 Electrically tunable lens 24

1.7.2 Electrowetting lens 25
1.7.3 Multi-actuator adaptive lens 26
1.8 Control systems 27
1.8.1 Closed loop 28
1.8.2 Wavefront sensorless optimisation 29

2 Propagation of a wavefront and Curvature Sensing 33
2.1 Theory of wavefront curvature sensing 33
2.1.1 Solution of the ITE by Fourier transform 34
2.1.2 Solution of the ITE by finite difference method 35
2.2 Simulation of an aberrated signal 35
2.3 Algorithm of the wavefront curvature sensor 36
2.4 Results of the simulations 37
2.4.1 Uniform beam 37
2.4.2 Gaussian beam 42

3 Wavefront curvature sensor 49
3.1 Experimental setup 49
3.2 Results 52

4 Control of the multi-actuator lens 57
4.1 Theory of the control 57
4.2 Experimental validation 59

5 Fluorescence Microscopy and Depth Reconstruction 71
5.1 Fluorescence 71
5.2 Fluorescence microscopy 74
5.3 Total internal reflection fluorescence microscopy 75
5.4 Confocal microscopy 76

5.5 Single molecule microscopy 77
5.6 Z-coordinate reconstruction with astigmatic wavefront on a microscope 79

Conclusions **89**

A Irradiance Transport Equation **91**

B Matlab Codes **97**

Bibliography **111**

Introduction

This thesis is focused on the development of a wavefront curvature sensor and the wavefront correction with a multi-actuator lens developed at CNR-IFN of Padua. The curvature sensor determines the wavefront from two images taken out of the focus of a telescope and is typically used when working with point-like objects, as for example with stars in astronomy. Our goal is to obtain the depth of point-like objects in a specimen by using out of focus images to characterise the deformation of the object due to astigmatism.

In the first chapter we discuss the optical image formation and how to represent a wavefront with two different bases. We then discuss the components of an adaptive optics system and we introduce three different wavefront sensors, several wavefront correctors and three kinds of control systems. Among the wavefront correctors, the multi-actuator lens is of particular importance, since it allows to modify a wavefront with several aberrations.

In the second chapter we introduce the theory of the curvature sensing and we present the results of an algorithm that estimates the wavefront by using two out of focus images.

The third chapter contains the laboratory test of the wavefront curvature sensor.

In the fourth chapter we show how it is possible to control the multi-actuator lens with out of focus images and to obtain an almost flat wavefront by using this particular approach. The practical implementation is then exposed with two different setups.

In the last chapter we use the multi-actuator lens mounted on a fluorescence microscope to obtain depth reconstruction of a sample by using a single image with an astigmatic wavefront.

Chapter 1

Aberrations and adaptive optics

In an ideal imaging system, rays coming from a point like object are focused by the optic system into another point of the image plane. However, ideal conditions do not exist and when the rays travel through a medium and then through the system they come to be affected by aberrations. For example, if a spherical wave is emitted by a point-like sorgent under ideal conditions, when the wave passes through the system it remains spherical with its centre in the image plane. However, if there are misalignments and imperfections in the system, or even dust in the propagation medium, the wave can no longer be spherical.
For example, astronomers always come to deal with aberrations on telescopes due to atmosphere. In fact, the wavefront produced by a star is plane until it reaches the atmosphere of the Earth. Here different refractive indices modify the wavefront, so that it results no to be plane anymore when it is detected by the telescope.
Adaptive optics [5],[14] enables to correct the wavefront. In the astronomical case the adaptive optics system enables to make the wavefront flat. In this chapter, we will introduce some basic concepts of optical imaging and wavefront formations. Later on, we will discuss adaptive optics and its typical components: wavefront sensors, control systems and wavefront correctors.

1.1 Optical image formation

An aberration introduced into the pupil of the objective lens can be expressed as a wavefront function $W(x, y)$, measured in waves, or a phase function $\Phi(x, y) = 2\pi W(x, y)$, measured in radians. The wavefront function represents the difference between the physical wavefront and the reference wavefront that can be sphere or plane. The complex pupil function can be written as

$$P(r, \theta) = P(r)e^{i\Phi(x,y)}, \tag{1.1}$$

where $P(r) = 1$ in the unit circle, 0 elsewhere.

In an optical system with spatially incoherent light, the image irradiance $I(u, \nu)$ is the convolution of the object irradiance $I_0(\eta, \xi)$ with the point spread function (PSF) $|h(u, \nu)|^2$ of the system:

$$I(u, \nu) = \int\int |h(u - \eta, \nu - \xi)|^2 I_0(\eta, \xi)\ d\eta\ d\xi = |h(u, \nu)|^2 \otimes I_0(u, \nu). \tag{1.2}$$

The PSF describes the response of an incoherent imaging system to a point source, and it is mathematically equivalent to the modulus squared of the amplitude point spread function $h(u, \nu)$. Using the scalar diffraction theory we can write the amplitude point spread function as

$$h(u, \nu) = \frac{1}{\lambda z} \int\int P(x, y)e^{-i\frac{2\pi}{\lambda z}(ux+\nu y)} dxdy = \frac{1}{\lambda z}\mathcal{F}\{P(x, y)\}_{f_x=\frac{u}{\lambda z}, f_y=\frac{\nu}{\lambda z}} \tag{1.3}$$

where z is the image distance and $\mathcal{F}\{...\}$ is the Fourier transform operation.

If we want to describe the aberrations that affect a system, it is useful to express the wavefront as a complete and orthogonal series of polynomials, as we can see in the next sections.

1.2 Zernike polynomials

Zernike polynomials are used to represent a wavefront in a circle domain. In fact these polynomials are a basis in the unit circle, that it means that they are a set of orthonormal functions. If we indicate with $Z_n^m(\rho,\theta)$ the Zernike polynomial of order (n,m), we can write it as

$$Z_n^m(\rho,\theta) = \begin{cases} \sqrt{n+1}\; R_n^m(\rho)\cos(m\theta) & \text{for } m > 0 \\ \sqrt{n+1}\; R_n^m(\rho)\sin(m\theta) & \text{for } m < 0 \\ \sqrt{n+q}\; R_n^0(\rho) & \text{for } m = 0 \end{cases} \tag{1.4}$$

where ρ and θ are polar coordinates. The function $R_n^m(\rho)$ can be written as

$$R_n^m(\rho) = \sum_{k=0}^{\frac{n-m}{2}} \frac{(-1)^k (n-k)!}{k!\left(\frac{n+m}{2}-k\right)!\left(\frac{n-m}{2}-k\right)!}\rho^{n-2k} \tag{1.5}$$

for $n-m$ even, whereas it takes constant value 0 if $n-m$ odd.
The orthogonality law of Zernike polynomials states that

$$\iint Z_n^m(\rho,\theta) Z_{n'}^{m'}(\rho,\theta)\mathrm{d}\rho\mathrm{d}\theta = \delta_{n,n'}\delta_{m,m'}. \tag{1.6}$$

Usually the wavefront is not expressed with this indexation. Let us look at Figure 1.1, where Zernike polynomials are represented in a triangular scheme where the $i-th$ row is given by all polynomials Z_n^m with $n=i$. We relabel them in order of appearence in the scheme (top to bottom, left to right). In the first row we thus have Z_1 (piston), in the second row Z_2 (tip) and Z_3 (tilt), in the third row Z_4 (oblique astigmatism), Z_5 (defocus), Z_6 (vertical astigmatism) and so on. Using this indexation, a wavefront can be written as

$$W(\rho,\theta) = \sum_{i=1}^{\infty} c_i Z_i(\rho,\theta). \tag{1.7}$$

A remarkable property that descends from the orthogonality law is that the wavefront variance between the wavefront we have and the one we wish to obtain can be easily calculated as

$$\sigma^2 = \sum_{i=2}^{\infty} c_i^2. \tag{1.8}$$

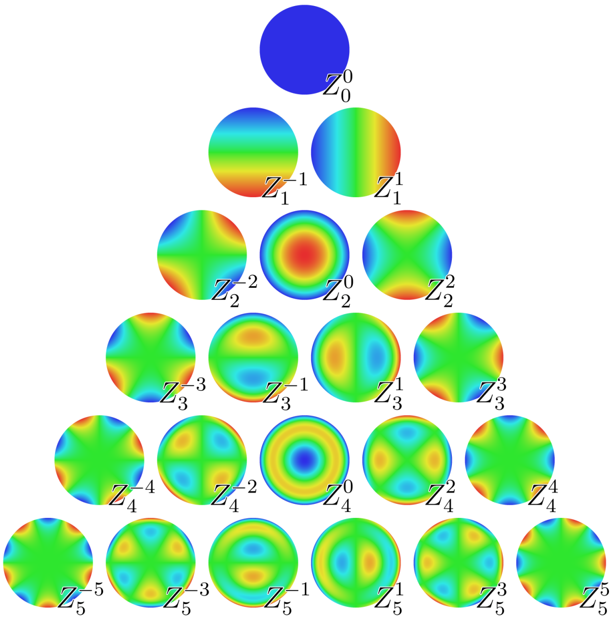

Figure 1.1: Zernike polynomials up to 5-th order.

1.3 Lukosz polynomials

The wavefront can also be expressed with other basis, and the Lukosz polynomials are an example of it If we indicate with $Z_n^m(\rho,\theta)$ the Lukosz polynomial of order (n,m), we can write it as

$$L_n^m(\rho,\theta) = \begin{cases} B_n^m(\rho)\cos(m\theta) & \text{for } m \geqslant 0 \\ B_n^m(\rho)\sin(m\theta) & \text{for } m < 0, \end{cases} \tag{1.9}$$

where

$$B_n^m(\rho,\theta) = \begin{cases} \frac{1}{2\sqrt{(n)}}\left(R_n^0(\rho) - R_{n-2}^0(\rho)\right) & \text{for } n \neq m = 0 \\ \frac{1}{2\sqrt{(n)}}\left(R_n^m(\rho) - R_{n-2}^m(\rho)\right) & \text{for } n \neq m \neq 0 \\ \frac{1}{\sqrt{(n)}}\left(R_n^n(\rho)\right) & \text{for } n = m \neq 0 \\ 1 & \text{for } n = m = 0. \end{cases} \tag{1.10}$$

The term $R_n^m(\rho)$ is the same of equation 1.5.

As in the previous case, instead of using n and m, we can use the index i to refer to the polynomials. Using this different indexation, the wavefront can be written as

$$W(\rho,\theta) = \sum_{i=1}^{\infty} a_i L_i. \tag{1.11}$$

The orthogonality law satisfied by these polynomials is rather different from Zernike ones. In fact the latter is given by

$$\frac{1}{\pi}\iint \big(\nabla L_{i_1}\big)\cdot\big(\nabla L_{i_2}\big)\rho d\rho d\theta = \delta_{i_1,i_2}. \tag{1.12}$$

Now we write the root mean square (rms) of a certain ensemble of values $\{x\}$,

$$x_{rms} = \sqrt{\frac{\sum_{i=1}^{N}(x_i-\bar{x})}{N^2}}, \tag{1.13}$$

where $\bar{x}$ is the average value and N the number of values. An interesting property of Lukosz polynomials is that they can give a simple expression for the root mean squared radius. in fact, it is defined as

$$\rho_{rms}^2 = \langle(\Delta x)^2 + (\Delta y)^2\rangle, \tag{1.14}$$

where Δx and Δy are the transverse aberrations, which are equal to

$$\Delta x = R\lambda\frac{\partial W(x,y)}{\partial x}, \tag{1.15}$$

$$\Delta y = R\lambda\frac{\partial W(x,y)}{\partial y}. \tag{1.16}$$

The coefficient λ is the wavelength and R is the radius of the reference sphere. Using Equations 1.11 and 1.12, we can show that ρ_{rms}^2 is proportional to the squares of the Lukosz coefficients:

$$
\begin{aligned}
\rho_{rms}^2 &= (R\lambda)^2 \langle \left(\frac{\partial W(x,y)}{\partial x} \right)^2 + \left(\frac{\partial W(x,y)}{\partial y} \right)^2 \rangle \\
&= (R\lambda)^2 \langle |\nabla W(x,y)|^2 \rangle \\
&= (R\lambda)^2 \langle \nabla W(x,y) \cdot \nabla W(x,y) \rangle \\
&= (R\lambda)^2 \sum_{i=4}^{\infty} \sum_{j=4}^{\infty} a_i a_j \langle \nabla L_i(x,y) \cdot \nabla L_j(x,y) \rangle \\
&= (R\lambda)^2 \sum_{i=4}^{\infty} \sum_{j=4}^{\infty} a_i a_j \frac{1}{\pi} \iint \nabla L_i(\rho,\theta) \cdot \nabla L_j(\rho,\theta) \rho d\rho d\theta \\
&= \left(\frac{\lambda}{2\pi NA} \right) \sum_{i=4}^{\infty} a_i^2,
\end{aligned}
$$

where NA is the numerical aperture of the system, and in the last step a change from polar to cartesian coordinates has been made.

1.4 Maréchal criterion

We have seen that the variance of the wavefront, expressed as sum of Zernike polynomials, is quite simple to calculate. This is of great advantage, since it can be used to compute the Strehl intensity

$$S = 1 - \sigma^2, \tag{1.17}$$

which let us determine the quality of the optical system according to the Marèchal criterion. This latter states that a system is well corrected if

$$S \geq 0.8. \tag{1.18}$$

This means that if the rms between the wavefront we measure and the flat wavefront is less or equal than 0.08 *waves*, the wavefront can be considered as flat.

1.5 Wavefront sensors

The problem of measuring the wavefront is very common in optics and different types of wavefront sensors (WFS) have been developed to solve it. The most used are the Shack-Hartmann, the curvature, the pyramid and the phase diversity wavefront sensor.

1.5.1 Shack-Hartmann WFS

The Shack-Hartmann WFS is composed by a detector and an array of lenslets each having the same focal length. Every lens takes a small part of the signal and focuses it on the detector, typically a CCD. If we record an image of a plane wave and one of an aberrated wave, the local tilt of the wavefront across each lens can be calculated by using different positions of the spots of the two images. Since any phase aberration can be approximated by a set of discrete tilts, by sampling an array of lenslets it is then possible to approximate the whole wavefront by using all the measured tilts. Therefore, the sensor measures the tilt over each aperture by comparing the measured positions of the aberrated spots to the position of the spots for a reference input beam. The tilt measurements are then converted into the estimated wavefront.

1.5.2 Curvature WFS

In the curvature sensor the wavefront is reconstructed by using two different images. The signal is focused by a lens and the two images are taken out of the focus of the same quantity, one before and one after the focus. More details of this type of sensor are in Chapter 2.

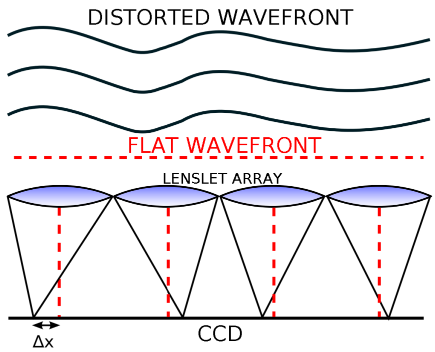

Figure 1.2: Scheme of a Shack-Hartmann wavefront sensor. When the wavefront is flat the focused spots are in the intersection between the CCD and the red dotted lines. When the wavefront is aberrated, the focused spots on the CCD translate with respect to the flat wavefront's spots.

1.5.3 Pyramid WFS

This kind of wavefront sensor was invented by Ragazzoni in 1994 [12]. It is similar to the Shack-Hartmann. A pyramidal glass prism is placed in front of a lens. The prism divides the signal beam in four parts and the lens projected the four parts in a detector. The difference in intensity over the four images contains information about the first derivatives of the incoming wavefront.

1.5.4 Phase diversity WFS

With this kind of sensor we need to take two images of the object, one with a known defocus distance with respect to the other, as shown by Gonsalves [7], [9], [8]. The method Gonsalves presents in 1976 is an iterative method to retrieve the phase of a pair of light distributions. We know the width of the pupil, so we generate a random phase and calculate the PSF. We then define a merit function and minimise it by using an algorithm that search the phase. Typically the algorithm to find the phase is a steepest descend one or a genetic algorithm. Finally, when the merit function is minimised, the phase is uniquely determined.
Some years before Gonsalves, Gerchberg and Saxton [6] presented in 1972 a method

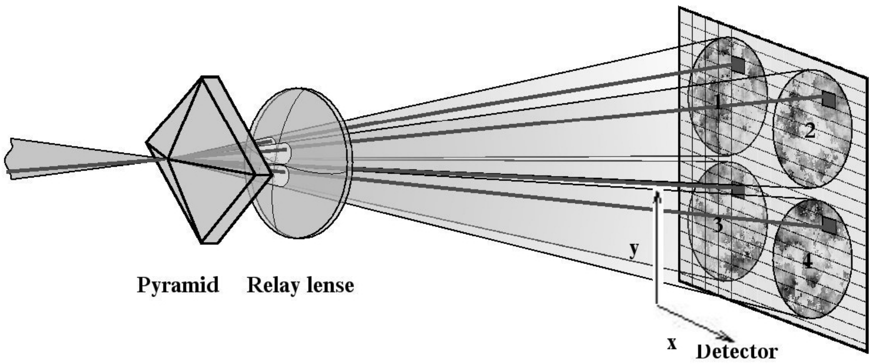

Figure 1.3: Scheme of a pyramid wavefront sensor.

to obtain the phase by using the intensity of the sampled image and diffraction plane. To find the phase, a random number generator is used to generate an array of random numbers between π and $-\pi$ which serves as the initial estimate of the phases corresponding to the sampled image amplitudes. These amplitudes are multiplied by the respective sampled image amplitudes. The Fourier transform is then applied to these new values and the phases obtained trnasform are combined with the corresponding sampled diffraction plane amplitudes. These values are then inverse Fourier transformed, the phases of the sample points computed and combined with the sampled image amplitudes to form a new estimation of the image amplitudes and the process is repeated.
However, the Gerchber-Saxton algorithm is very slow and Fienup [3] the year later presented other methods that are faster than the previous. Fienup et al. made a comparison between the curvature sensor and the phase diversity too [4].

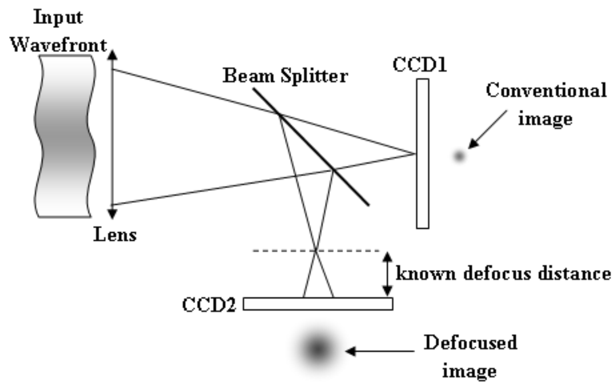

Figure 1.4: Scheme of a phase diversity wavefront sensor.

1.6 Wavefront correctors: Deformable Mirrors

Deformable mirrors (DMs) are mirrors whose reflecting surface can be deformed by attaching on its backsome. Deformable mirrors are the most used wavefront correctors. These type of correctors do not introduce chromatic aberration and thanks to high reflective coatings they allow not to lose signal. The principal parameters that describe a deformable mirror are:

- the number of actuators, that determines the number of degree of freedom of the system. The greater is the number of actuators, the higher order of aberrations the deformable mirror can resolve.
- the actuator pitch, that is the distance between actuators' centres.
- the actuator stroke, that is the maximum actuator displacement from the initial position.
- the response time, that can vary from microseconds to tens of seconds.
- the hysteresis, that is the positional error from previous actuator position commands and it obviously affects the ability of the mirror to work in a predictable way.

- the influence matrix, which contains information on how the actuators affect the shape of the surface. Usually the influence matrix is calculated by setting the actuators to a certain value one at a time and the wavefront obtained is recorded by a wavefront sensor. If we call the influence matrix A, the wavefront Φ is given by

$$\Phi = Ac, \tag{1.19}$$

where c is the vector commands to be applied to the actuators. Once we know the wavefront and the influcence matrix, we can invert Equation 1.19 to obtain the vector commands, that is

$$c = A^{-1}\Phi. \tag{1.20}$$

1.6.1 Segmented DMs

These type of mirrors are formed by some independent flat mirrors, each one with an actuator on its back. The actuators can move up and down (piston) and/or allow the mirror on the top of them to rotate (tip/tilt). By using a segmented DM there is no crosstalk between the actuators, because each one is independent to the others. Segmented DMs allow to reach high dimensions, in fact they are usually mounted in big telescopes. A great disadvantage is that they are expensive.

Figure 1.5: A segmented deformable mirror with piston and tip/tilt actuators.

1.6.2 Continuous faceplate DMs

These mirrors are similar to the segmented DMs. However, in this case there is not a flat mirror for each actuator, but only one deformable continuous faceplate on the top of all the actuators. The shapes that this mirror can assume depend on the combination of the forces applied by the actuators, the boundary condition of the faceplate and the properties of the faceplate itself. Therefore in this case there is crosstalk between the actuators.

Figure 1.6: Scheme of a continuous deformable mirror.

1.6.3 Membrane DMs

The membrane DMs use the same continuous faceplate as the previously presented mirrors. In this case, instead of by the actuators, the membrane is moved with electrode pads by using electrostatic pressure. The electrostatic pressure exerted by the i-th electrode can be written as

$$p_i = \frac{\epsilon_0}{2}\left(\frac{V_i}{d}\right)^2, \tag{1.21}$$

where V_i is the voltage applied and d is the distance between the electrode and the membrane. Pressure can only be positive, so we have to choose a bias zero position of the voltage, usually $V_{max}/\sqrt{2}$, that allows us to create positive and negative aberrations by moving up and down the membrane.

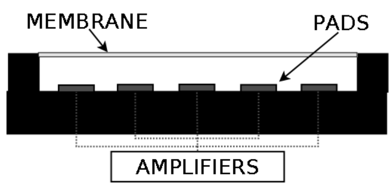

Figure 1.7: Scheme of a membrane deformable mirror.

1.6.4 Bimorph DMs

Bimorph mirrors also use a continuous faceplate, but the actuators are flat disks of piezoelectric material bonded to the back of the faceplate, as we can see in Figure 1.8. By changing the voltage of the piezoelectric materials, their dimensions change parallel to the faceplate, and this produces bending moments that curve the faceplate. Typically these kinds of mirrors are produced with low-cost materials and very well suited to adaptive optics systems.

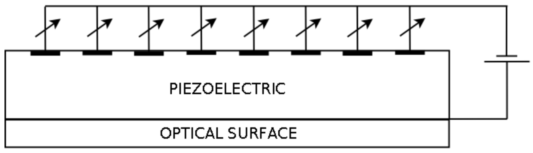

Figure 1.8: Scheme of a bimorph deformable mirror.

1.6.5 Microelectromechanical DMs

Microelectromechanical (MEM) DMs are a quite new technology for cheap DMs. These devices are derived from the membrane DMs, and the peculiarity is that these DMs are small, so that they can be used in very small devices. The dimension of the components is typically between 1 and 100 μm, thus the whole deformable mirror is no bigger than 1 cm and it contains hundreds or thousands of actuators. MEMs actuators are moved with electrostatic forces as in membrane DMs, but in this case voltage is very small, tens of Volts, and so is the current.

1.7 Wavefront correctors: Deformable Lenses

In the last few years deformable lenses (DLs) have been developed to perform wavefront correction. DLs are very interesting because they enable to minimise the dimension of the adaptive optics setup. Here we present different types of deformable lenses.

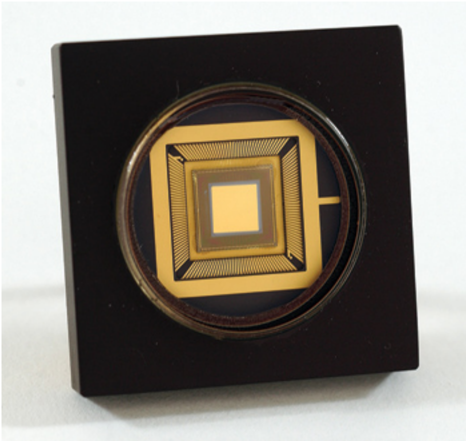

Figure 1.9: A MEM deformable mirror.

1.7.1 Electrically tunable lens

The first lens we introduce is the electrically tunable lens created by Optotune (model EL 10-30) [11]. It has an external diameter of 30 mm and a clear aperture of 10 mm, and it is 10.75 mm thick. It consists of a container (two thin glass windows with a $400 - 700$ nm broad band), which is filled with a low dispersion transparent liquid (with refractive index $n = 1.300$) and sealed off with an elastic polymer membrane. This lens has an electromagnetic actuator that changes the pressure of the liquid. By varying the current of the actuator we can change the pressure applied to the liquid and therefore change the focal length of the lens.

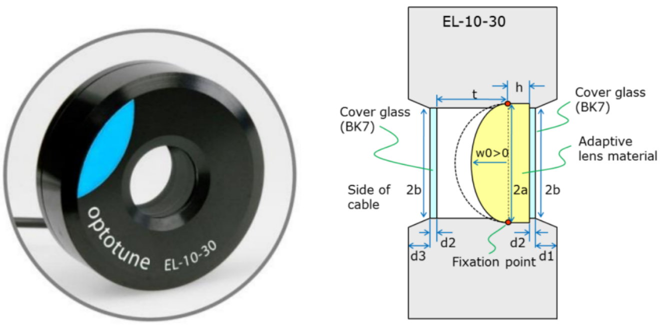

(a) (b)

Figure 1.10: Optotune lens. Photo of the lens (a) and scheme (b).

1.7.2 Electrowetting lens

Electrowetting is the change of the solid-electrolyte contact angle due to an applied voltage between the solid and the electrolyte.
The shape of a liquid-vapour interface on a solid is determined by the Young-Laplace relation, and the theoretical description descends from thermodynamic considerations between the three phases: solid, liquid and vapour. If we indicate with γ the interfacial energy, i.e the surface tension, we will have three surface tensions: γ_{SL} between the solid and the liquid, γ_{LG} between the liquid and the vapour and γ_{SG} between the solid and the vapour. The Young-Laplace equation is then (see Figure 1.11)

$$\gamma_{SG} - \gamma_{SL} - \gamma_{LG} \cos\theta_C = 0, \tag{1.22}$$

from which we get the contact angle

$$\theta_C = \arccos\left(\frac{\gamma_{SG} - \gamma_{SL}}{\gamma_{LG}}\right). \tag{1.23}$$

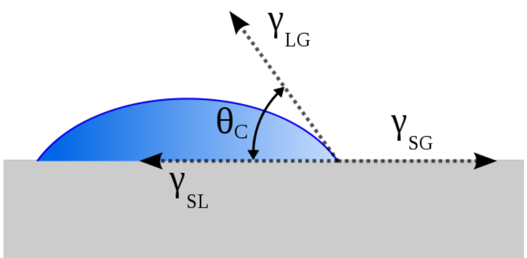

Figure 1.11: Scheme of the contact angle.

If the liquid is an electrolyte, the surface tension of the solid conductor and the electrolyte depend on the voltage applied according to the law

$$\gamma_{SL} = \gamma_{SL_0} - \frac{CV^2}{2}, \tag{1.24}$$

where γ_{SL_0} is the surface tension at 0 V, C is the capacitance of the interface and V is the potential. The contact angle is then

$$\cos\theta_C = \frac{\gamma_{SG} - \gamma_{SL_0} + \frac{CV^2}{2}}{\gamma_{LG}}. \tag{1.25}$$

An electrowetting lens [22] uses this principle to obtain a lens that can change its shape from plano-convex to plano-concave. A typical electrowetting lens is composed by a cylindrical insulant box whose bases are made of glass. Inside the box there are the solid conductor and the electrolyte, as it is shown in Figure 1.12.

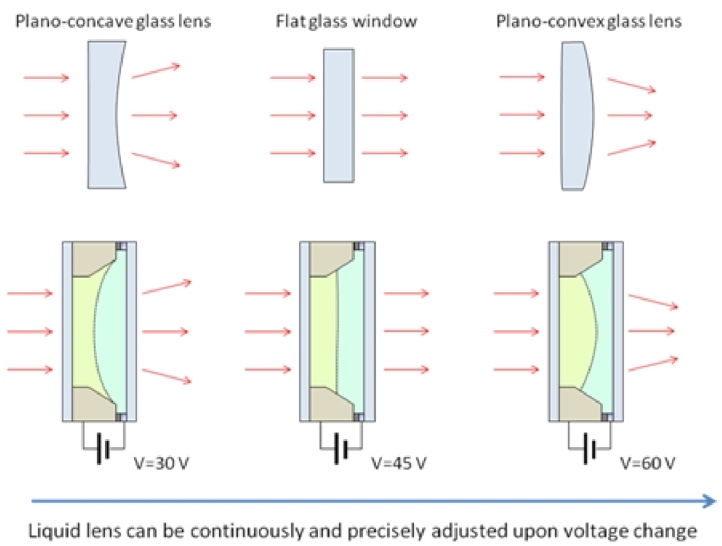

Figure 1.12: The electrowetting lens changes behaviour by varying the supply tension.

1.7.3 Multi-actuator adaptive lens

The last lens we introduce is a multi-actuator adaptive lens, invented by Bonora in 2014 [1]. It is composed of two thin glass windows (borosilicate glass, refractive index $n = 1.474$, 150 μm thick), upon each of which is mounted a piezoelectric actuator ring. The space between the windows is filled with a transparent liquid (Vaseline oil, refractive index $n = 1.475$). The piezoelectric actuator ring (Physics

Instruments) has an external diameter of 25 mm and an internal diameter of 10 mm with a thickness of 200 μm. The multi-actuator lens used has 9 independent actuators per ring, thus the total number of actuators is 18. The rings are glued to the windows and act as bimorph actuators: therefore the application of a voltage generates a bending of the glass windows. The actuators can be controlled using an high voltage (+/- 125 V) driver (Adaptica srl, IO64). As in the case of deformable mirrors, if we apply a voltage to one actuator at a time, we obtain the influence matrix of the system, and by inverting equation 1.19 we find the vector commands.

As we can see in Figure 1.13, the top and bottom actuators work in different ways.

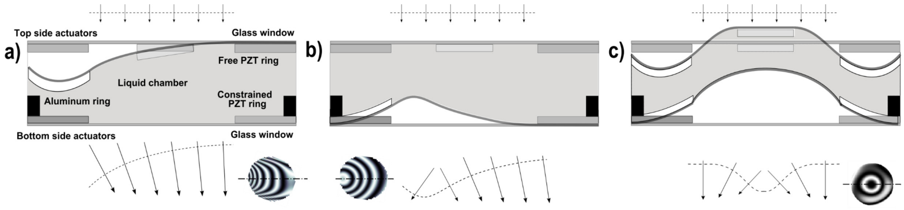

Figure 1.13: Layout of the multi-actuator adaptive lens. Panels a-c show the measured wavefront with the relative interferogram in three different configurations: a) one electrode on the top, b) one electrode on the bottom, c) all the actuators with the same voltage value.

In fact, the actuators on the top are free to move, instead the bottom actuators are blocked by a rigid aluminium ring. Thanks to this particular configuration, the bottom actuators are virtually inside the clear aperture, and this enables to correct wavefront aberrations up to the fourth order of the Zernike polynomials.

1.8 Control systems

There are three kinds of control of the adaptive optics system.

The first type of control is the open loop, where we directly use the measurements of the wavefront to control the actuators and eliminate the aberrations.

The second type of control is the closed loop. In this case we compare the desired wavefront with the measured one with a sensor, compute the error between them and use this error to control the actuators of the corrector.

The last type of control is called wavefront sensorless. In this case there is no wavefront sensor and the correction is possible by the optimisation of some properties of the signal.

1.8.1 Closed loop

The closed loop is the typical control for adaptive optics systems. Generally, in this kind of control an integrator is used to introduce memory in the system, thanks to which we keep trace of information about the previous corrections. The wavefront aberrations vector Φ in the $(k+1)$-th iteration can be written as

$$\begin{cases} \Phi_{k+1} = \Phi_k + Ac_k \\ y_{k+1} = \Phi_k + v_k, \end{cases} \tag{1.26}$$

where A is the influence matrix of the corrector, c the actuator commands vector, v is the measured noise vector and y the measured aberrations vector. In a discrete time approach, the integrator for the command vector is

$$c_k = -Ry_k + c_{k-1}, \tag{1.27}$$

where R is called reconstructor matrix and it has to be determined. To consider a wavefront corrected, Φ_{k+1} has to be null. The reconstructor can be found (setting $c_{k-1} = 0$) as

$$c_k = -Ry_k = -A^{-1}y_k \simeq -A^{-1}\Phi_k. \tag{1.28}$$

Since the influence matrix is not square, the simplest way to find the reconstructor is by using a least square technique, that results into

$$R = (A^T A)^{-1} A^T. \tag{1.29}$$

Other techniques can be used to calculate R, one of them is the already seen singular value decomposition. In this case

$$A = UWV^T, \tag{1.30}$$

and

$$R = VW^{-1}U^T. \tag{1.31}$$

Once we have computed the reconstructor, it is possible to implement the closed loop control system.

1.8.2 Wavefront sensorless optimisation

As already described, in the sensorless optimisation [24], [13] the wavefront sensor is not used, and the image is corrected maximising a metric with the wavefront corrector. In literature several imaging sharpness metrics are described. For example, two optimisation metrics have already been introduced, the Strehl intensity and the rms spot radius. However, they work only with point-like samples, so they cannot be properly considered as metrics. For extended samples, the most used metric is the irradiance squared metric, proposed by Buffington and Muller in 1974 [10]. The irradiance squared metric is defined as

$$IQ = \iint I(x, y)^2 dxdy, \tag{1.32}$$

where $I(x, y)$ is the irradiance. In the article it is demonstrated that this metric is maximised when the wavefront distortions are zero and that the maximum is global. Moreover, in the same article other metrics are defined, for example

$$S_\beta = \iint I(x, y)^\beta \qquad \text{for } \beta = 3, 4 \tag{1.33}$$

$$S_5 = \iint I(x, y) \ln \big(I(x, y)\big) dxdy \tag{1.34}$$

$$S_5 = \iint I(x,y)(x^2+y^2)dxdy \tag{1.35}$$

Another metric that it is largely used is the spectral density metric (SD), proposed by Debarre, Booth and Wilson in 2007 [2]. This metric is based on the lower spatial frequency of the image, but leads to a correction of all the frequencies of the image, specially for incoherent images. SD metric is defined as

$$SD = \int_{\xi=0}^{2\pi} \int_{m=M_1}^{M_2} S_J(m)\ m\ dm\ d\xi, \tag{1.36}$$

where $S_J(m)$ is called spectral density and can be calculated as follows. If we apply the convolution theorem to Equation 1.2 we obtain

$$I(x,y) = |h(x,y)|^2 \otimes I_0(x,y). \tag{1.37}$$

Now we apply the Fourier transform to this equation and multiply for the complex conjugate, so the result is

$$S_J(m) = |\mathcal{F}\{h(x,y)^2\}|^2 \cdot |\mathcal{F}\{I_0(x,y)\}|^2, \tag{1.38}$$

where $S_J(m) = |\mathcal{F}\{I(x,y)\}|^2$.

SD metric has some interesting property. The first one is that it reaches the maximum in a free aberrations system. Moreover, we can select the spatial frequencies to use in equation. The bigger is the range of frequencies, the larger the aberrations that can be corrected in the image. If we consider only low spatial frequencies and samples without a predominant periodicity in one direction, it has been demonstrated that SD metric can be written as a series of Lukosz coefficients,

$$SD = \frac{1}{q_1 + q_2 \sum_{i=4}^{\infty} a_i^2}, \tag{1.39}$$

where q_1 and q_2 are positive constants that depend on (M_1, M_2) fixed. If we take the inverse relation, SD^{-1} is a paraboloid in N dimensions, with a global minimum in the free aberrations system configuration,

$$SD^{-1} = q_1 + q_2 \sum_{i=4}^{\infty} a_i^2. \tag{1.40}$$

Once we have chosen the basis and the metric, we need to use an algorithm to perform the optimisation. A possible algorithm is the modes correction, that uses the inverse of the SD metric to correct every single Lukosz mode and it is faster than any other algorithm in this field. The steps to follow are:

1. Evaluate SD_0^{-1} with the wavefront corrector relaxed.

2. Select the number of modes N to correct and a bias term b to add and subtract to every mode.

3. Excluding piston, tip and tilt that do not contribute to the aberration, calculate the inverse SD metric of the given Lukosz mode with coefficient $+b$.

4. Repeat the same calculation with coefficient $-b$.

5. We now have three points, which let us extrapolate the parabola to find the value that corrects the aberration of the given Lukosz mode, that is

$$a_{corr} = \frac{-b(SD_+^{-1} - SD_-^{-1})}{2SD_+^{-1} - 4SD_0^{-1} + 2SD_-^{-1}} \tag{1.41}$$

6. With the value a_{corr} the given Lukosz mode is correct and we can then change Lukosz mode and repeat the same steps until all the N modes are corrected.

Chapter 2

Propagation of a wavefront and Curvature Sensing

In this chapter we present the theory for a numerical wavefront propagation and for a wavefront curvature sensor, developed by F. Roddier in 1988 [15, 16, 17].

2.1 Theory of wavefront curvature sensing

Let us suppose to have a wavefront focused by a lens with focal length f. The curvature sensing consists of the detection of two images with one or two detectors and an algorithm that elaborates a combination of these images. If we use two detectors, one takes a snapshot of the irradiance distribution I_1 in a plane orthogonal to the optic axis at a distance l before the focus of the lens. The other one detects the irradiance distribution I_2 at a distance l after the focus (see Figure 2.1).

We can write the irradiance transport equation (ITE) (see Appendix A) as

$$\frac{\partial I}{\partial z} = -\left(\nabla I \cdot \nabla W + I \nabla^2 W\right), \tag{2.1}$$

where z is the direction of the optic axis, I is the irradiance and W the wavefront. We apply this equation at the pupil plane ($z = 0$), where we assume the illumination to be fairly uniform and equal to I_0 inside the pupil and 0 outside. In this

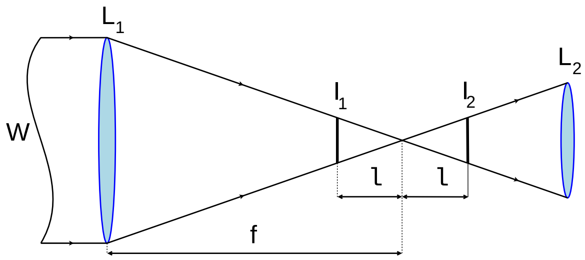

Figure 2.1: Scheme of a wavefront curvature sensor. The wavefront W propagates and passes through the two lenses L_1 and L_2. The two irradiances I_1 and I_2 are different if the wavefront is not plane, so we can extrapolate information of the incoming wavefront using I_1 and I_2.

plane $\nabla I = 0$ everywhere but at the pupil edge, where

$$\nabla I = -I_0 \hat{n} \delta_{edge}. \tag{2.2}$$

In this equation $\hat{n}\delta_{edge}$ is a ring delta function around the edge of the signal. Putting Equation 2.1 into 2.2 yields

$$-\frac{1}{I_0}\frac{\partial I}{\partial z} = \nabla^2 W + \delta_{edge}\frac{\partial W}{\partial \hat{n}}. \tag{2.3}$$

The longitudinal derivative normalised by I_0 can be approximated as

$$-\frac{1}{I_0}\frac{\partial I}{\partial z} = \frac{1}{\Delta z}\frac{I_1 - I_2}{I_1 + I_2}, \tag{2.4}$$

where $I_1 = I(z - \Delta z) = I_0 - \frac{\partial I}{\partial z}\Delta z$, $I_2 = I(z + \Delta z) = I_0 + \frac{\partial I}{\partial z}\Delta z$ and $\Delta z = \frac{f(f-l)}{2l}$. If we constrain $\frac{\partial W_{edge}}{\partial \hat{n}} = 0$, the equation we have to solve is simpler than that in Equation 2.1:

$$\nabla^2 W = -\frac{1}{\Delta z}\frac{I_1 - I_2}{I_1 + I_2}. \tag{2.5}$$

2.1.1 Solution of the ITE by Fourier transform

Equation 2.5 can be solved by using the Fourier transform. In fact it is well known that

$$W(x,y) = \int_{-\infty}^{+\infty}\int_{-\infty}^{+\infty} W(\xi,\eta) e^{-i2\pi(\xi x + \eta y)}\, \mathrm{d}\xi \mathrm{d}\eta. \tag{2.6}$$

Therefore if we apply the Fourier transform to the laplacian of the wavefront we obtain

$$\mathcal{F}_{\xi,\eta}\{\nabla^2 W(x,y)\} = -4\pi^2(\xi^2+\eta^2)\mathcal{F}_{\xi,\eta}\{W(x,y)\}, \tag{2.7}$$

where ξ and η are the spatial frequencies that range from $-\frac{1}{2pxsz}$ to $+\frac{1}{2pxsz}$ and $pxsz$ is the aperture pixel size, typical of each experiment. If we now combine Equations 2.5, 2.7 and apply the inverse Fourier transform ($\mathcal{F}^{-1}$) we can finally calculate the wavefront

$$W = \mathcal{F}^{-1}_{x,y}\left\{\frac{\mathcal{F}_{\xi,\eta}\left\{-\frac{1}{\Delta z}\frac{I_1-I_2}{I_1+I_2}\right\}}{-4\pi^2(\xi^2+\eta^2)}\right\}. \tag{2.8}$$

2.1.2 Solution of the ITE by finite difference method

Another method to calculate the wavefront from Equation 2.5 is by using a finite difference algorithm [23]. In this case we solve the Poisson equation numerically on a square grid with equal steps δ_{xy} in the two directions of the grid x and y. The grid knots are indexed as i and j for x and y respectively. The grid approximation of the Laplace operator takes the form

$$\nabla^2 W = \frac{W_{i+1,j}+W_{i-1,j}+W_{i,j+1}+W_{i,j-1}-4W_{i,j}}{\delta_{xy}^2}. \tag{2.9}$$

If we combine Equations 2.5 and 2.9 we finally obtain

$$W_{i,j} = -\frac{1}{4}\Big(\delta_{xy}^2 - \frac{1}{\Delta z}\frac{I_1-I_2}{I_1+I_2} - W_{i-1,j} - W_{i+1,j} - W_{i,j+1} - W_{i,j-1}\Big). \tag{2.10}$$

Starting with matrices of zeros as initial conditions we iteratively compute $W_{i,j}$ according to the previous formula, until a minimum stationary error is reached.

2.2 Simulation of an aberrated signal

The simulation of an aberrated wavefront has been made to test the software of the wavefront curvature sensor. To perform this simulation we have written a software

in MATLAB that creates an aberrated wavefront and then propagates it through a lens to obtain two out of focus images I_1 and I_2.
The aberrated wavefront is calculated in term of Zernike modes and the optical field can be in a uniform or a gaussian beam. The optical field can be written as

$$U(x_1, y_1) = f(x_1, y_1)e^{iW(x_1,y_1)}, \tag{2.11}$$

where $W(x, y)$ is the aberration, $f(x, y)$ is a function that represents the gaussian beam or the uniform beam and $i = \sqrt{(-1)}$ is the imaginary unit. After the optical field is generated, it propagates through a lens, and the optical field after the lens can be written in Fraunhofer conditions as

$$U(x_2, y_2) = \frac{1}{i\lambda f_l} e^{i\frac{k}{2f_l}(x_2^2+y_2^2)FT\{f(x_1,y_1)\}}, \tag{2.12}$$

where λ is the wavelength, k the wave vector and f_l the focal length of the lens. In order to use the wavefront curvature sensor, the optical field cannot be in the focus of the lens but out of it. Therefore we added and subtracted the same quantity of the fifth Zernike mode (defocus) to $W(x_1, y_1)$ in Equation 2.12.

2.3 Algorithm of the wavefront curvature sensor

The wavefront reconstruction has been done in different steps:

1. Obtain the out of focus images I_1 and I_2.
2. Create the signal $S = -\frac{I_1 - I_2}{I_1 + I_2}$.
3. Find the size of the mask.
4. Calculate the wavefront by using Equations 2.8 or 2.10.
5. Set $\frac{\partial W}{\partial n} = 0$ on the boundary.

6. Estimate sensor signal S by applying the Laplace operator to W according to the equation $\nabla^2 W = S_2$.

7. Replace the signal S_2 lying inside the mask into S and come back to point 4.

8. When RMS reaches a minimum, stop the algorithm: W has been found. To calculate the RMS we used the formula

$$RMS = \sqrt{\frac{\sum_{i=1}^{N} (W_i^{calc} - W_i^{real})^2}{N^2}}, \tag{2.13}$$

where N is the number of points of the wavefront grid, W^{calc} is the wavefront obtained by the algorithm and W^{real} is the real wavefront used in the propagation program.

2.4 Results of the simulations

We created aberrated images in two different beams. In what follows we analysed them separately.

2.4.1 Uniform beam

Now we propose an example of the analysis with some Zernike modes. The out of focus images for the uniform beam with Zernike polynomial 14 can be seen in Figure 2.2. Then we used the described algorithm in Section 2.3 to obtain an estimation of the wavefront.

An example of the beginning signal $S = -\frac{I_1 - I_2}{I_1 + I_2}$ is shown in Figure 2.3. The size of the mask depends on the dimension of the defocused signal without aberration. We computed the width of these signals in pixels. Once we obtained this parameter, we varied the dimension of the mask and calculated the RMS between

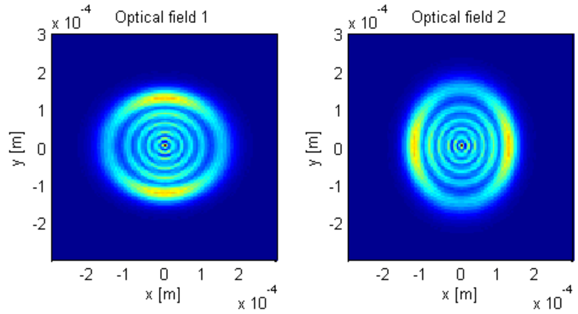

Figure 2.2: Optical fields of a wavefront with mode fourteen (Z_{14}). The left image is the optical field out of focus before the lens, while the right image after the lens.

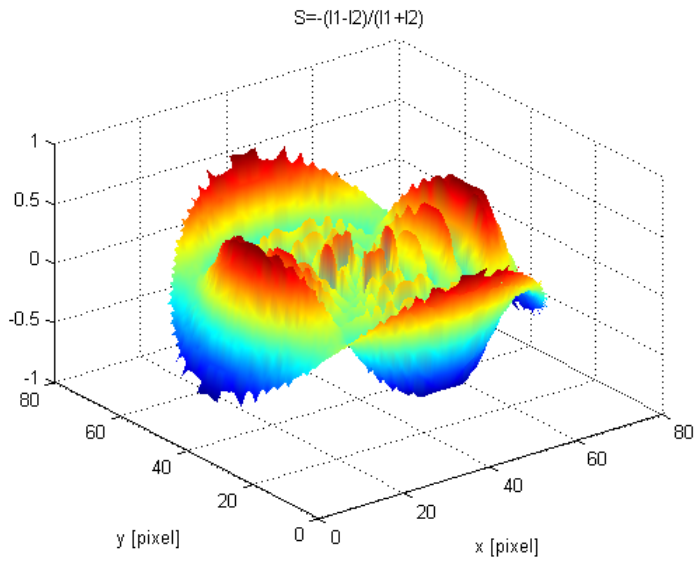

Figure 2.3: Signal S obtained by I_1 and I_2 with mode 14.

the computed wavefront and the real wavefront. We also computed the spectral purity of the Zernike coefficients obtained by the algorithm. When both the minimum of the RMS and the maximum of the spectral purity were found, we used the corresponding size of the mask for the linear trend analysis. As we can see in Figure 2.4 the minimum of the RMS for several Zernike coefficients is where the diameter of the mask is 72 pixels. In order to validate the size of the mask, we also used the spectral purity of the coefficient, that it is defined as

$$SP = \sqrt{\frac{c^2}{\sum_{i=1}^{N} c_i^2}}, \tag{2.14}$$

where c is the estimation of the WCS algorithm of the Zernike coefficient used in the propagation and the denominator is the squared sum of all the Zernike coefficients obtained by the WCS.

We can observe in Figure 2.5 that the maximum value of the spectral purity is assumed at the same size of the mask of the minimum of the RMS, thus we used that diameter for the analysis of the linearity. The spectral purity for two analysed modes, 4 and 11, is practically always near one. This is due to the fact that when the mask of these two modes exceeds a particular value, the wavefront does not change shape anymore and the only value that changes is the peak to valley of it.

Since the signal $S = -\frac{I_1 - I_2}{I_1 + I_2}$ can assume values from -1 to $+1$, when it reaches these extrema the signal will be saturated. If we vary the coefficient of the aberration in the propagation, we can observe the estimation of the coefficient in the WCS algorithm, to see that it saturates over a certain value.

As we can see in Figure 2.6, the linear trend is correct up to a coefficient value of 2.8 *waves*, that is when the signal reaches the extrema -1 or $+1$. In Figure 2.7 there is an example of a saturated signal.

The saturation can be reduced if the out of focus distance is smaller. Nevertheless, if we reduce this distance, the WCS algorithm will be less sensitive to the change

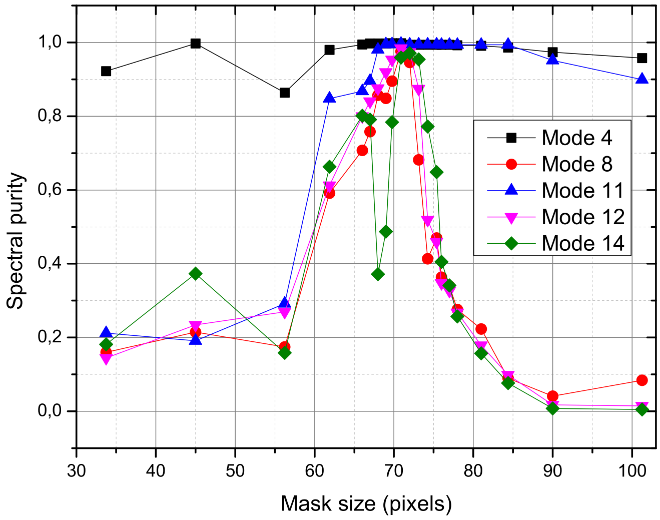

Figure 2.4: RMS between the real wavefront and the computed wavefront in the uniform beam.

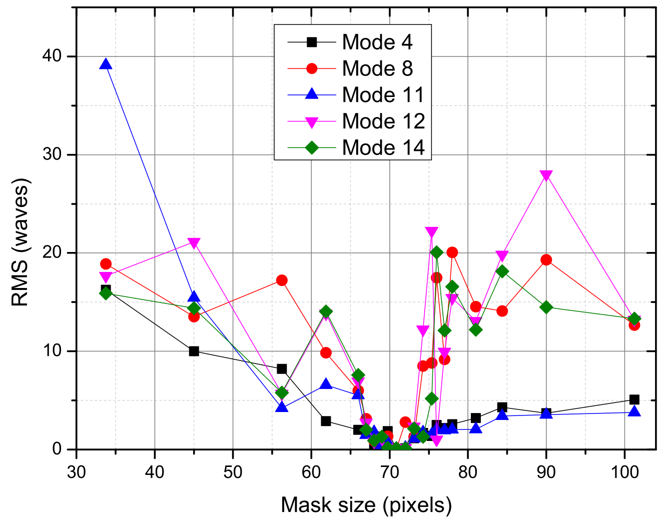

Figure 2.5: Spectral purity of the computed wavefront in the uniform beam.

of shape of the wavefront. On the other hand, if we want to increase the sensitivity to the aberrations, we will have to increase the out of focus distance, consequently the signal will saturate sooner.

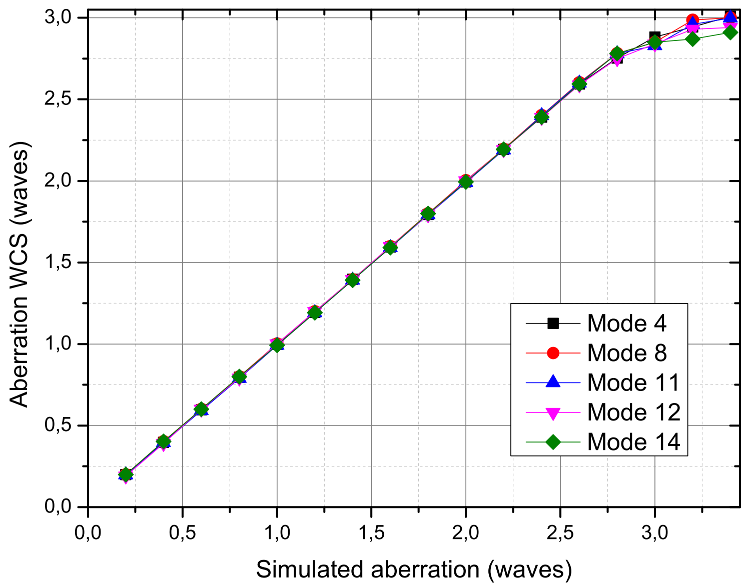

Figure 2.6: Linearity trend for three Zernike modes in an uniform beam.

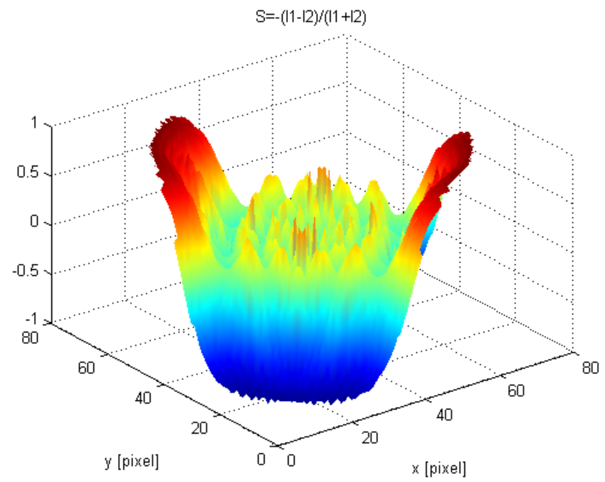

Figure 2.7: Saturation of the signal S with a coefficient of 3 *waves* for the fourth mode (astigmatism).

2.4.2 Gaussian beam

As in the previous case, we propose an analysis of several Zernike modes. The out of focus images for the gaussian beam of the mode 14 can be seen in Figure 2.9. Once we created these images, we have used the algorithm in Section 2.3 to obtain an estimation of the wavefront.

An example of the beginning signals $S = -\frac{I_1 - I_2}{I_1 + I_2}$ is represented in Figure 2.10.

The diameter of the mask depends on the dimension of the defocused images without aberration, as in the previous case. We calculated the full width at half maximum (FWHM) of the out of focus images and extrapolated the σ. Once we obtained this parameter, we varied the size of the mask in unit of σ and calculated the RMS between the computed wavefront and the real wavefront. Again we also computed the spectral purity of the Zernike coefficients obtained by the algorithm. When both the minimum of the RMS and the maximum of the spectral purity were found, we used the size of the corresponding mask for linear trend analysis. As we can see in Figure 2.11, the minimum of the RMS for several Zernike coefficients

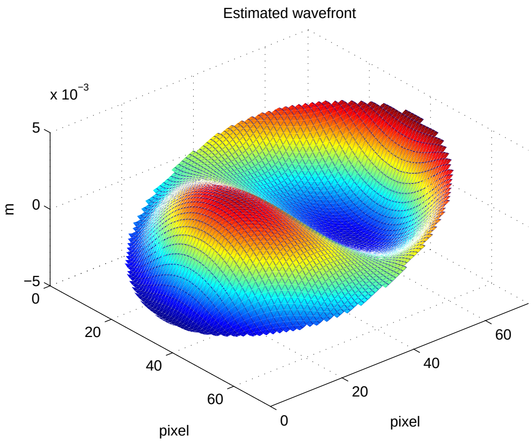

(a)

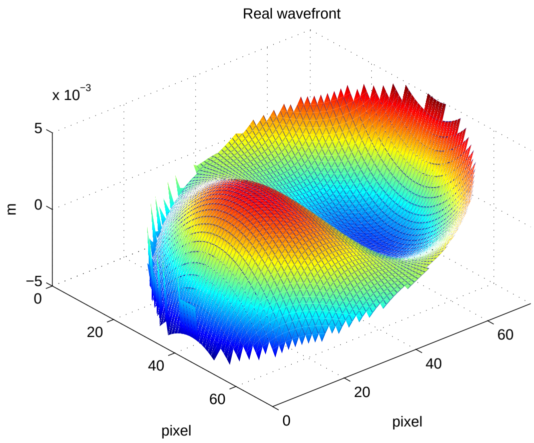

(b)

Figure 2.8: Example of an aberrated wavefront in uniform beam. On the top the estimated wavefront by the FFT algorithm, on the bottom the real wavefront given as input of the software of propagation.

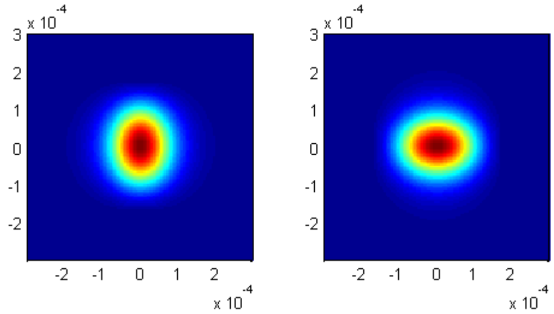

Figure 2.9: Optical fields of a wavefront with the fourteenth mode. The left image is the optical field out of focus before the lens, while the right image after the lens.

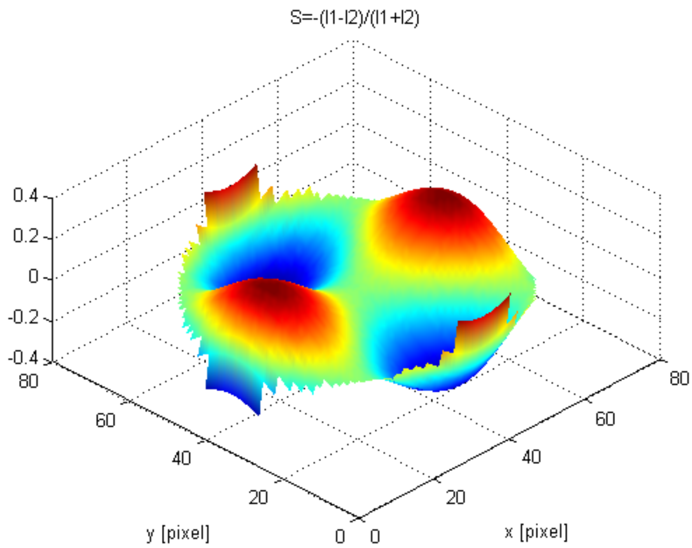

Figure 2.10: Signal S obtained by I_1 and I_2 with mode 14.

is where the diameter mask is 1.30σ, and the same value is assumed when the spectral purity is maximum (Figure 2.12), so we used this size of the mask for the analysis of the linearity.

The signal is calculated as in the uniform beam, $S = -\frac{I_1 - I_2}{I_1 + I_2}$, thus it assumes

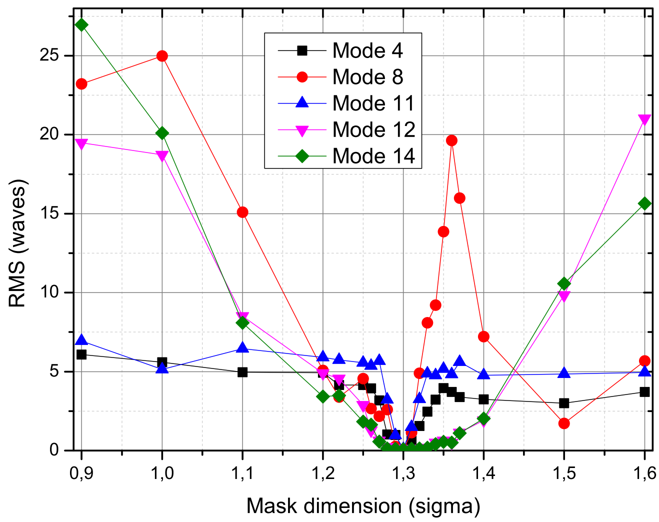

Figure 2.11: RMS between the real wavefront and the computed wavefront in the gaussian beam.

values from −1 to +1, and when it reaches these extrema the signal will be saturated. If we vary the coefficient of the aberration in the propagation software, we can see that the estimation of the coefficient in the WCS algorithm over a certain value does not change anymore: at that value the signal is saturated.

As we can see in Figure 2.13, the linear trend is correct up to a coefficient value of 3.0 *waves*, value over which the signal reaches the extrema −1 or +1, as it is well represented in Figure 2.14.

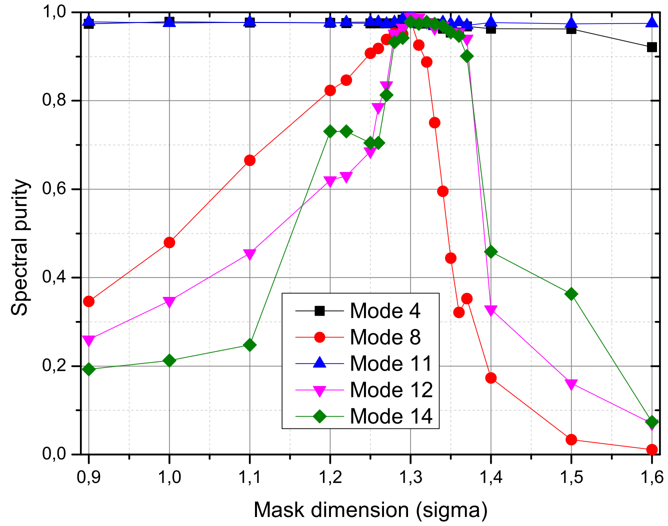

Figure 2.12: Spectral purity of the computed wavefront in the gaussian beam.

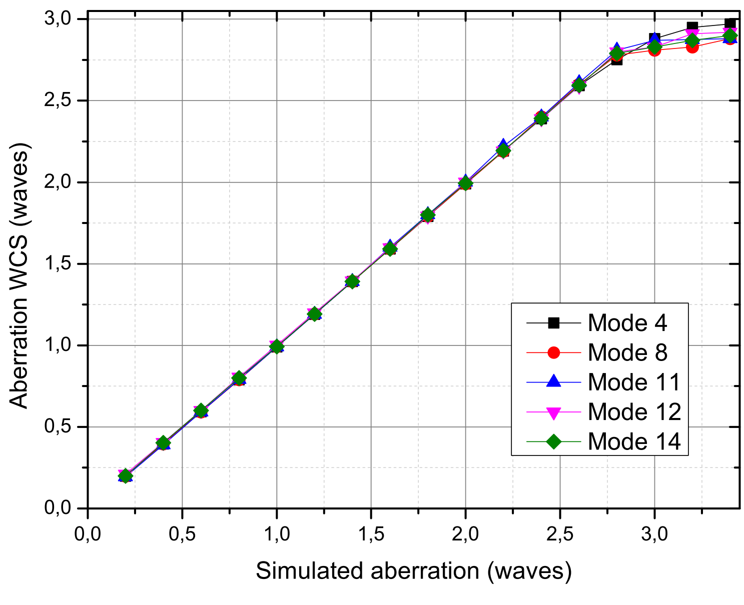

Figure 2.13: Linearity trend for several Zernike modes in a gaussian beam.

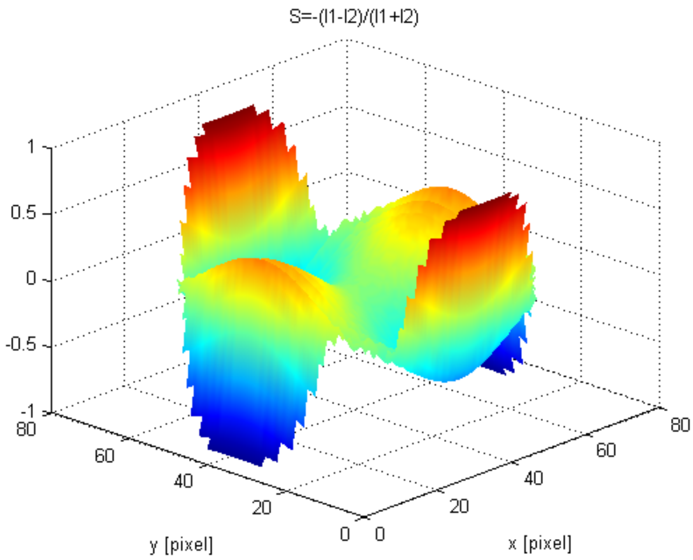

Figure 2.14: Saturation of the signal S with a coefficient of 3 *waves* for the fourteenth mode.

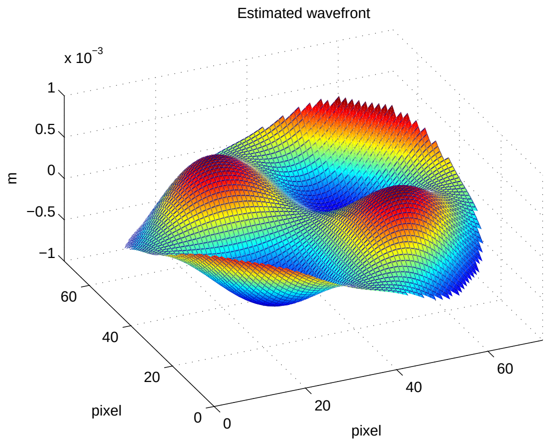

(a)

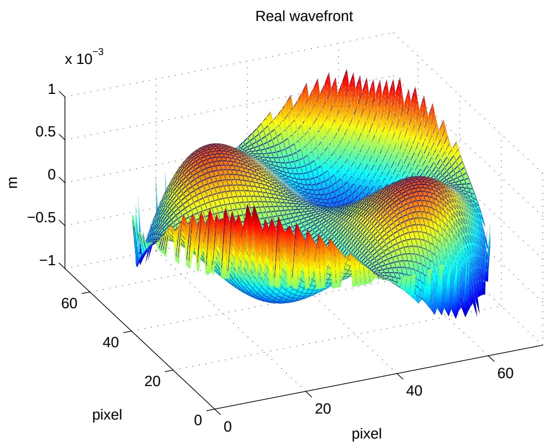

(b)

Figure 2.15: Example of an aberrated wavefront in a gaussian beam. On the top the estimated wavefront by the FFT algorithm, on the bottom the wavefront given as input in the software of propagation.

Chapter 3

Wavefront curvature sensor

3.1 Experimental setup

In laboratory we tested the wavefront curvature sensing algorithm by using the apparatus in Figure 3.1. It is composed of a laser with $\lambda = 670\ nm$, a lens of focal length $f_1 = 250\ mm$ which corrects to the infinity the laser, the multi-actuator lens with 18 actuators described in section 1.7, a telescope with ocular focal length $f_o = 250\ mm$ and eyepece with focal length $f_e = 100\ mm$. At the exit pupil of the telescope we set a Shack-Hartmann wavefront sensor, and out of the focus of the telescope we set a Thorlabs DCC1645C CMOS camera to record the images. We used a graduated scale to chose the out of focus positions of the camera.

We generated the wavefront with a particular aberration in closed loop by using the multi-actuator lens and the Shack-Hartmann WFS. Once we set the lens we recorded two images out of focus of the same quantity.

To perform the analysis of the recorded signal we had to choose the size of the mask and to set the spatial frequencies for the FFT. The size of the mask was chosen using geometrical considerations. We can calculate the clear aperture of the telescope as shown in Figure 3.3. We know the clear aperture of the lens, that is $10\ mm$, we can measure the focal length of the objective lens, f in the Figure, and the distance of the camera from the focus l. Therefore we can calculate also

d, according to

$$d = l \tan \alpha + l \tan \beta = \frac{lc}{f}. \tag{3.1}$$

We obtain the dimension in metre, but in MATLAB we work with pixels, so we have to divide it by the dimension of a single pixel of the CMOS camera, that is 3.6 μm.

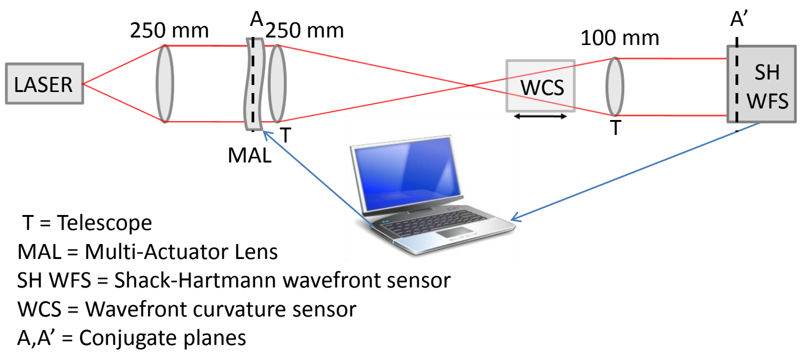

Figure 3.1: Scheme of the experimental setup.

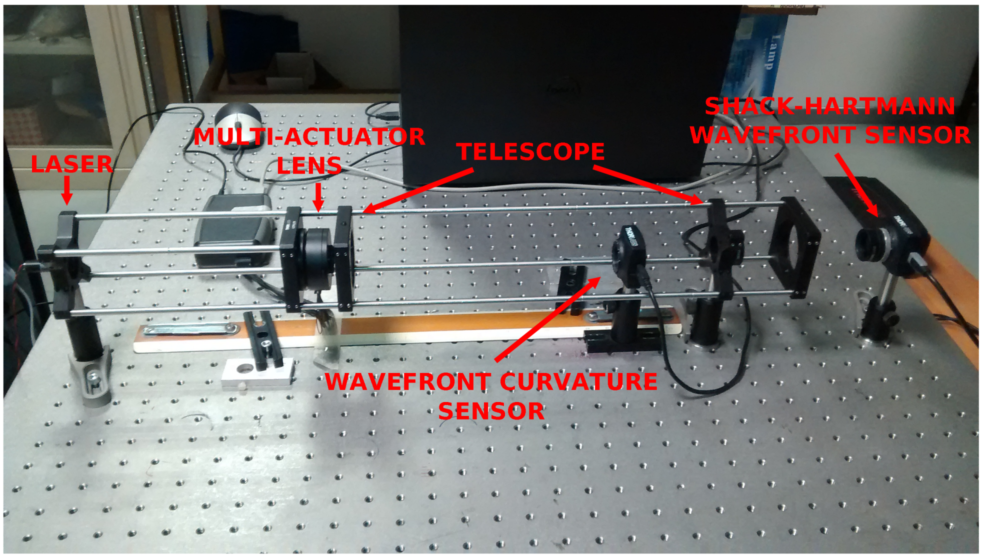

Figure 3.2: Picture of the experimental setup used to validate the curvature sensing algorithm.

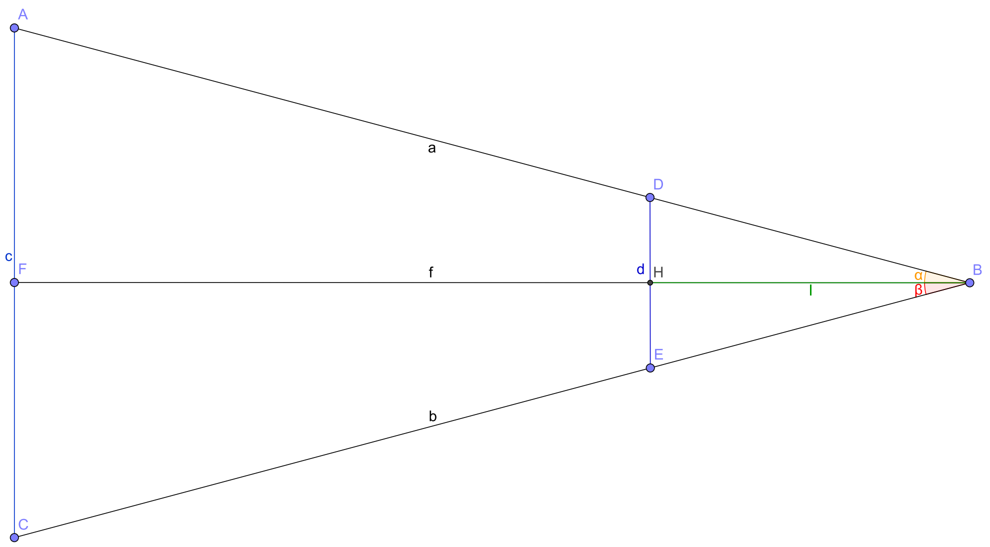

Figure 3.3: Scheme of the telescope: c is the clear aperture of the lens, B is the focus of the telescope and e is the focal length of the ocular. Clearly in our case $a = b$ and $\alpha = \beta$.

3.2 Results

As we have already pointed out in the previous chapter, the curvature sensing is linear until the signal S saturates. Moreover, if we acquire two out of focus pictures near the focus, the images are too small to contain enough information for the analysis. Therefore, we had to chose the out of focus distance to take the pictures, to balance the dimension of the images and to achieve a large linearity zone. In fact, these two requests are mutually exclusive: the bigger the out of focus distance, the greater the dimension of the image in pixels but also lower the sensitivity, since the difference of the images will saturate earlier. Vice versa, the shorter the out of focus distance, the smaller the size of the mask but also the higher the sensitivity, since the image will saturate later.

However, we had to use a single out of focus distance for both the requests, and after several trials we chose an out of focus distance of 5 mm. In the following pages we will show some analyses with different aberrations and the analysis of the linearity.

The first example is astigmatism. We used the closed loop to set astigmatism with coefficient of 0.3 $waves$.

In the second example in Figure 3.5 we used the eighth mode, with a coefficient set on the closed loop of 0.3 $waves$.

The next example is an aberration with the twelfth mode. We set the closed loop with a coefficient of 0.15 $waves$. The out of focus images recorded and analysed gave us the results in Figure 3.6.

The last example is spherical aberration. We set the closed loop to reach a spherical wavefront with coefficient of 0.1 $waves$. The out of focus images recorded and analysed gave us the results in figure 3.7.

All the analysed modes resulted to validate the algorithm. However, we remark

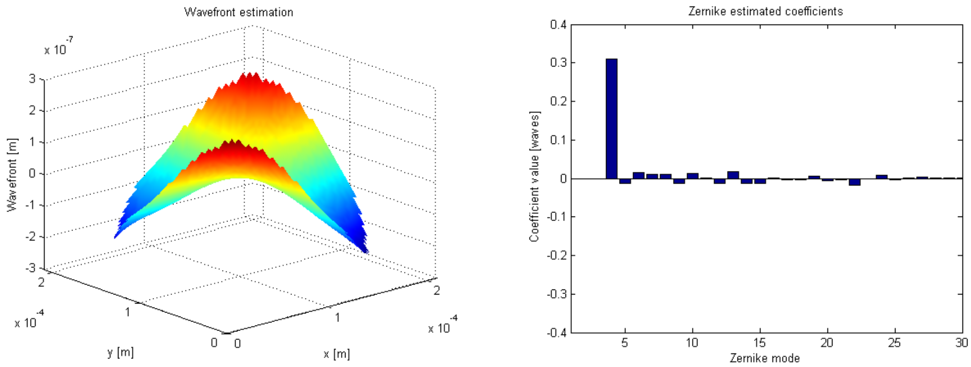

(a) (b)

Figure 3.4: Astigmatic aberration. In (a) the retrieved wavefront, in (b) the coefficients in *waves*.

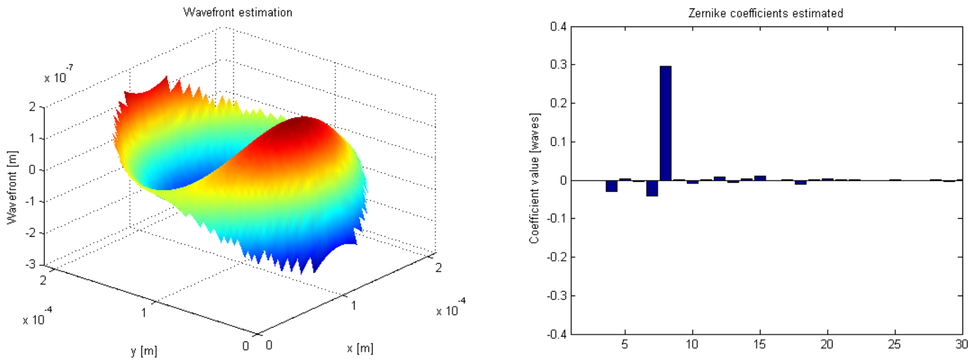

(a) (b)

Figure 3.5: Mode 8. In (a) the retrieved wavefront, in (b) the coefficients in *waves*.

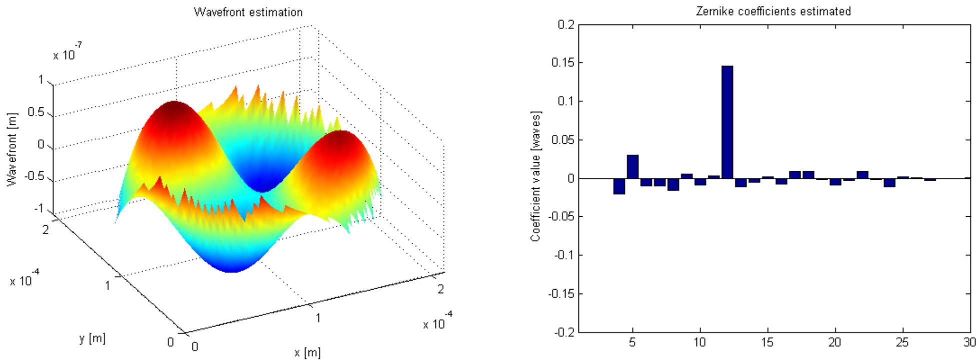

(a) (b)

Figure 3.6: Mode 12. In (a) the retrieved wavefront, in (b) the coefficients in *waves*.

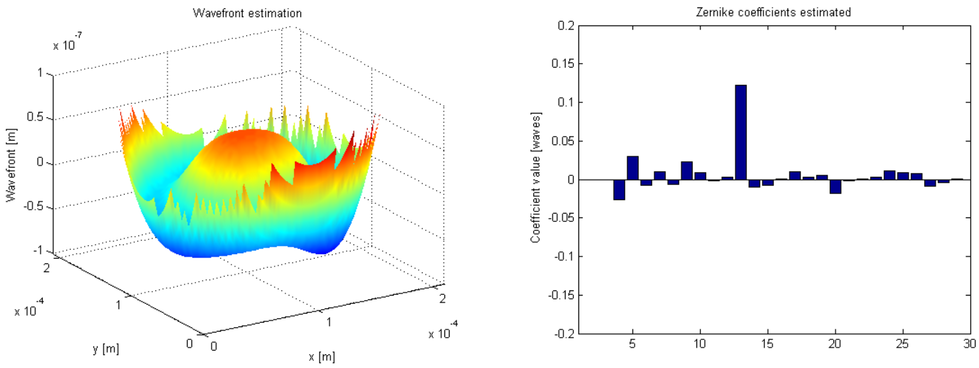

(a) (b)

Figure 3.7: Spherical aberration. In (a) the retrieved wavefront, in (b) the coefficients in *waves*.

that the retrieved wavefront and the corresponding estimated coefficients are not the same measured with the Shack-Hartmann wavefront sensor. This is because the focus of the telescope is not easily found, and only half of millimetre can cause the wrong retrieval of the wavefront. Moreover, we had problems with diffraction caused by laser light.

The linear trend of the wavefront curvature sensor is shown in Figure 3.8. As we can see over a value of 0.9 *waves* there is a loss of linearity, caused by the saturation of the signal $S = -\frac{1}{\Delta Z}\frac{I_1-I_2}{I_1+I_2}$ to the values $\frac{1}{\Delta z}$ and -$\frac{1}{\Delta z}$. The spectral purity of some Zernike coefficients is shown in Figure 3.9 and we can observe that it is over the 85% up to an amplitude of the coefficients of one wave. The result is quite good but on the other hand the spectral purity obtained with the Shack-Hartmann wavefront sensor is near 100% in all the cases.

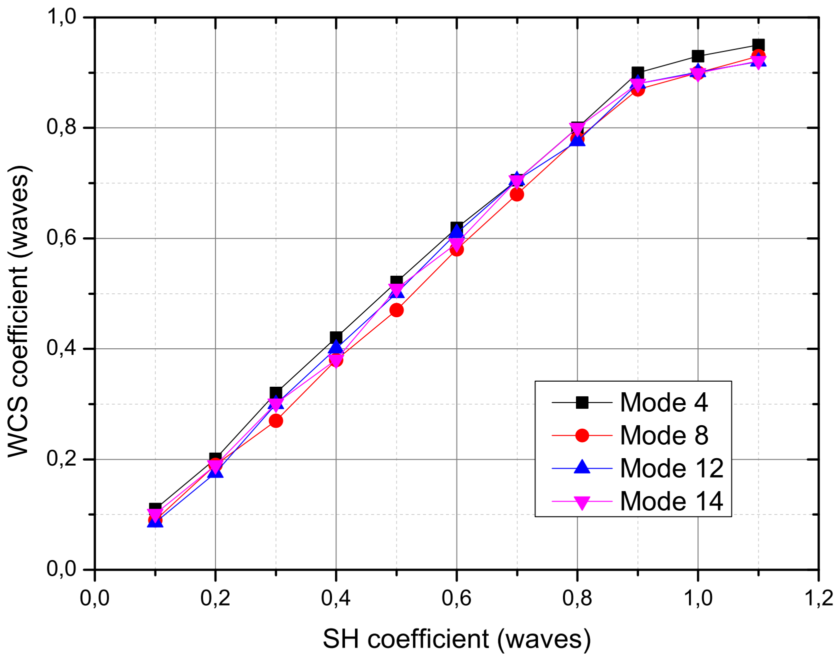

Figure 3.8: Linear trend of several Zernike coefficients.

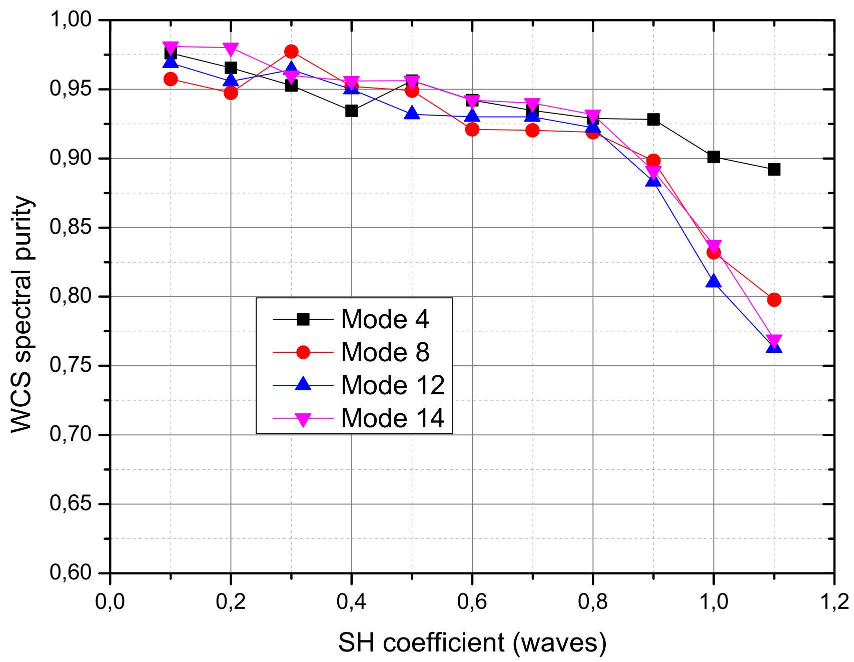

Figure 3.9: Spectral purity of several Zernike coefficients.

Chapter 4

Control of the multi-actuator lens

4.1 Theory of the control

As we have seen in Equation 2.1 the irradiance transport equation (ITE)

$$\frac{\partial I}{\partial z} = -\left(\nabla I \cdot \nabla W + I \nabla^2 W\right) \tag{4.1}$$

can be approximated as

$$\nabla^2 W \approx -\frac{1}{\Delta z}\frac{I_1 - I_2}{I_1 + I_2}. \tag{4.2}$$

On the other hand, if we have a piezoelectric material, there is a production of strain-inducing stress as the result of an applied electric field [20]. In fact, if we apply a voltage V to the piezoelectric material as in Figure 4.1, the displacement of the material is proportional to the electric field, and this latter is in turn proportional both to the voltage applied and the distance between the electrodes t. The variation of the length ΔL in the direction orthogonal of the applied voltage V is then

$$\Delta L = d\frac{VL}{t}, \tag{4.3}$$

where d is the piezoelectric deformation coefficient.

In our case, the shape of the membrane of the multi-actuator lens, that works with piezoelectric actuators, is then

$$S = bV_i, \tag{4.4}$$

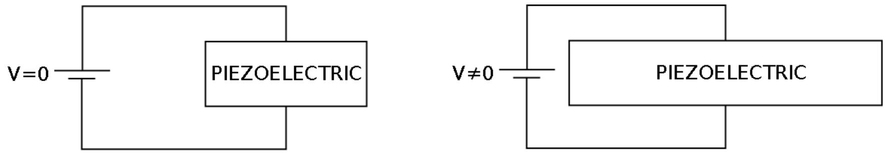

Figure 4.1: Piezoelectric material with zero and non-zero applied voltage.

where V_i is the voltage of the $i-th$ actuator and b contains the piezoelectric deformation coefficient and the dimensions L and t.
The shape of the lens is related to the wavefront according to

$$S = \nabla^2 W, \tag{4.5}$$

for the principle of the phase conjugation.
At this point if we combine Equations 4.2 and 4.4 we obtain the following relation [15, 19]:

$$\frac{I_1 - I_2}{I_1 + I_2} = kV, \tag{4.6}$$

where k is a multiplicative constant that we have to determine. Therefore we can record two out of focus images and use the combination of these two to find the correct voltage to be applied to the actuators.
Since we used the multi-actuator lens with 18 actuators, 9 in the internal zone and 9 in the external zone, we firstly had to find the region of interest of each actuator. We did it by using the influence matrix method obtained with the Shack-Hartmann wavefront sensor. An example of interferograms of influence matrix is shown in Figure 4.2. The computer driver that pilots the lens accepts an array of 18 elements, each one ranging from -1 to $+1$. In order to use the left-hand side of Equation 4.6 we had to know the multiplicative constant k. Thus we tried several values until we found the correct one by minimising the RMS between the obtained wavefront and the flat wavefront. Once we obtained the multiplicative constant, we calculated the correct voltage to apply and we repeated the procedure with a

Figure 4.2: Influence matrix of the multi-actuator lens.

new pair of I_1 and I_2 and so on until we reached the minimum aberration. The used algorithm was the following:

1. Obtain the images I_1 and I_2.

2. Create the signal $S = \frac{I_1 - I_2}{I_1 + I_2}$.

3. Find a mask in which make the calculations. The mask contains 18 regions, one for each actuator of the lens. This latter is set by using the influence matrix of the lens.

4. For every region of a single actuator the average value is calculated, so a value between -1 and $+1$ is found.

5. The 18 average values are converted in voltage, with a multiplicative constant k that minimises the RMS error between the estimated wavefront and the flat wavefront.

6. Repeat from the first point until the RMS reaches a minimum.

4.2 Experimental validation

We used the same setup of the previous chapter to perform a first experiment: a laser, a lens to correct to infinity, the multi-actuator lens and finally a telescope. The wavefront at the exit of the telescope was measured by a Shack-Hartmann

wavefront sensor and the camera to record the out of focus images was manually inserted and removed whether we needed one sensor or the other.
First we turned on the laser and "relaxed" the lens, that means we set the actuators to 0 V. In this condition we measured the wavefront with the Shack-Hartmann wavefront sensor and obtained the astigmatic wavefront in Figure 4.3.

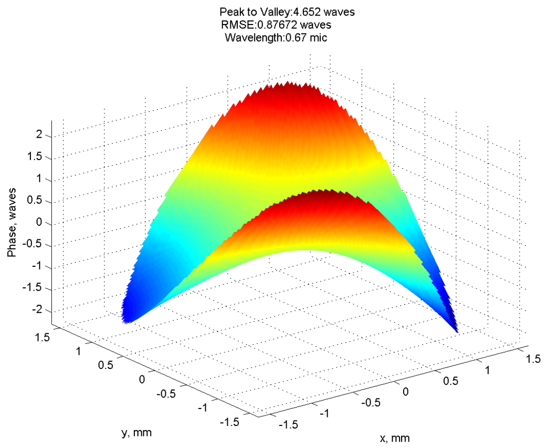

Figure 4.3: Wavefront of the relaxed lens. RMS error equal to 0.87672 *waves*.

We then placed the camera out of focus of 5 mm before and after the focus of the telescope, to obtain Figure 4.3.

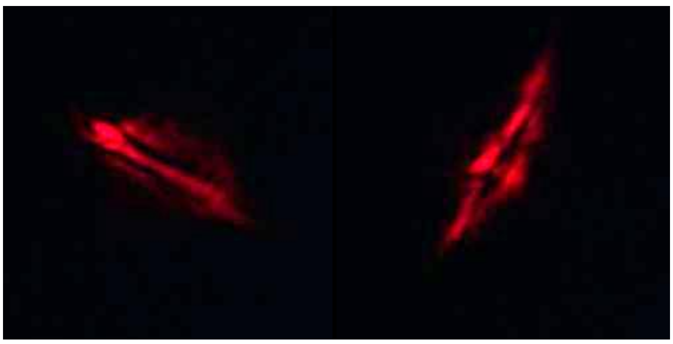

Figure 4.4: Out of focus images of the relaxed lens. On the left the image after the focus, on the right the image before the focus.

We calculated the left-hand side of Equation 4.6 and the mean value for each region of the corresponding actuator. We noticed that the first images were usually high-aberrated, thus the constant value that minimised the RMS was found to be high ($k = 1.8$). This is due to the fact that the first iteration had to eliminate the saturation of the signal $S = (I_1 - I_2)/(I_1 + I_2)$. To find the correct value we tried several values and the one that minimised the RMS error was selected. At this point we corrected the voltage value of the lens by subtracting at every actuator the corresponding obtained value. Then we measured again the wavefront with the Shack-Hartmann wavefront sensor and we recorded the two out of focus images.

Figure 4.5: Out of focus images after the first correction. On the left the image after the focus, on the right the image before the focus.

At this point the aberration was quite small, so after some tests we chose a value of the multiplicative constant equal to 0.36 and, with the same procedure of the first iteration, we calculated the voltage of every actuator and we corrected the lens consequently. Finally, after the wavefront estimation, we tried to record other two images but we didn't improve the RMS of the signal, because we reached the experimental limit of the setup. The final RMS error calculated with the Shack-Hartmann wavefront sensor, resulted to be 0.1103 *waves*, while the RMS error calculated with the curvature sensor resulted to be 0.1078 *waves*. In Figure 4.6 In Figure 4.7 two pictures of the spot in the focus before and after the correction are shown. In Figure 4.8 we plot the corresponding cross sections.

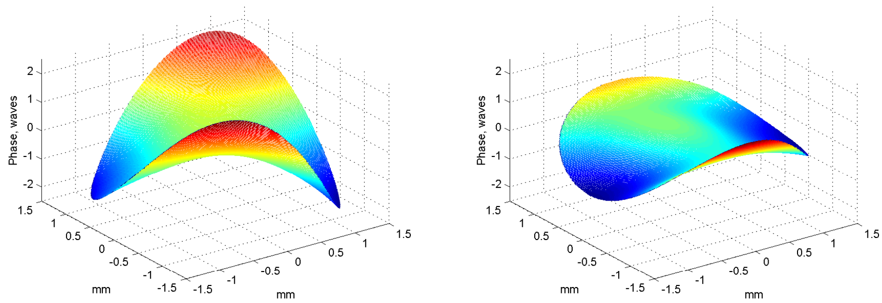

(a) (b)

Figure 4.6: Comparison of the initial (left) and final (right) wavefronts. Images obtained with the wavefront curvature sensor.

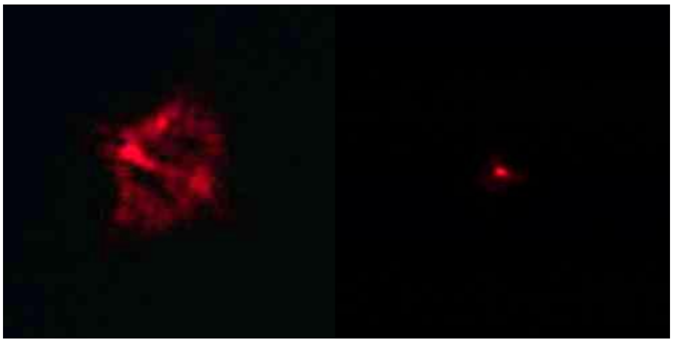

Figure 4.7: Focus spots of the laser before (left) and after (right) the correction with the multi-actuator lens.

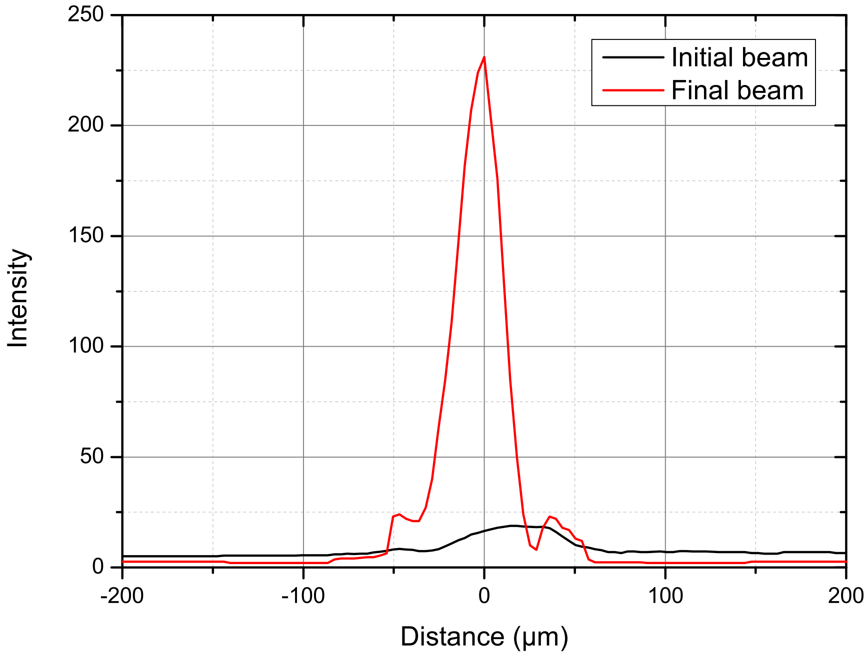

Figure 4.8: Horizontal cross section of the images in Figure 4.7.

To validate the curvature sensing control we used another setup. This latter used the multi-actuator lens to control the wavefront and a deformable mirror to create the aberration, as we can see in Figure 4.9. The apparatus consists of a non focused laser, a lens which corrects to the infinity the laser, the deformable mirror, a telescope to decrease the size of the beam of $2.5x$ to fit the clear aperture of the multi-actuator lens and another telescope of demagnification of $2.5x$ to fit the Shack-Hartmann wavefront sensor. Near the focus of the second telescope we inserted a beam splitter to allow the camera to take the out of focus images.

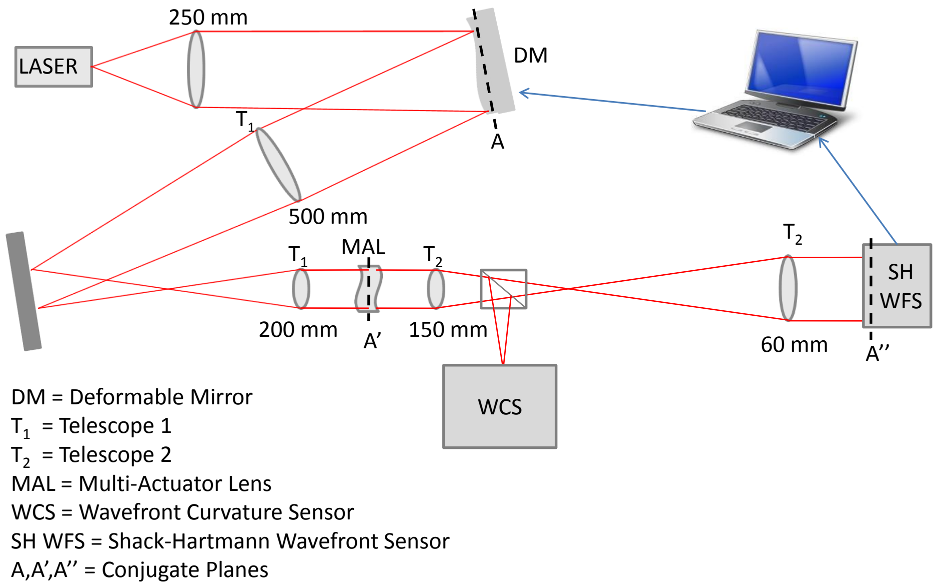

Figure 4.9: Second apparatus used to validate the curvature control.

In this case the deformable mirror changed the wavefront and the multi-actuator lens corrected it in order to obtain a flat wavefront.

In what follows we propose an example of this analysis, with initial out of focus images as in Figure 4.10.

The signal $S = -\frac{I_1 - I_2}{I_1 + I_2}$ is shown on top of Figure 4.11, while on bottom we can see the average value for every actuator.

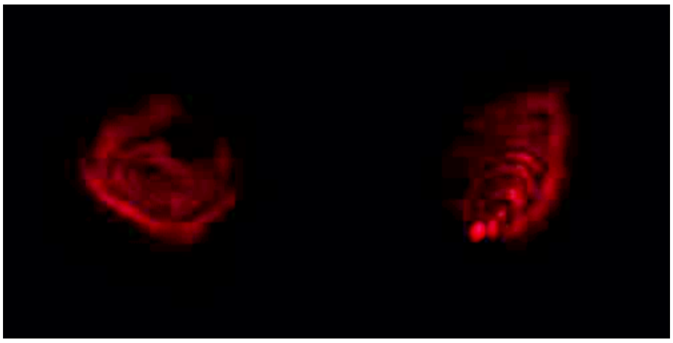

Figure 4.10: Out of focus images of the initial beam. On the left the image after the focus, on the right the image before the focus.

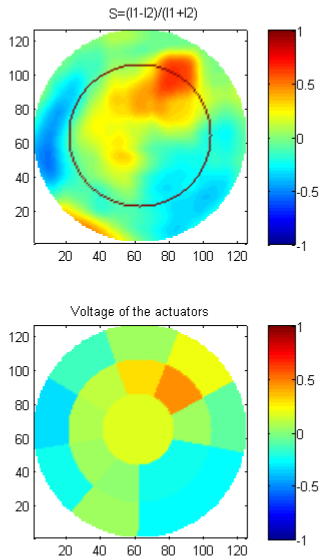

Figure 4.11: Signal S of the initial wavefront on the top and average value of the signal for every actuator on the bottom.

The initial RMS error calculated with SH wavefront sensor was 0.6142 *waves* while wi the curvature sensor 0.6106 *waves* it was .After the first iteration the wavefront measure with SH WFS had an RMS error of 0.13987 *waves*, and the multiplicative constant that minimised the RMS was chosen to be 1. The out of focus images in Figure 4.12 were used as input for the second iteration, and the signal for the actuator is shown in Figure 4.13. For the second iteration we

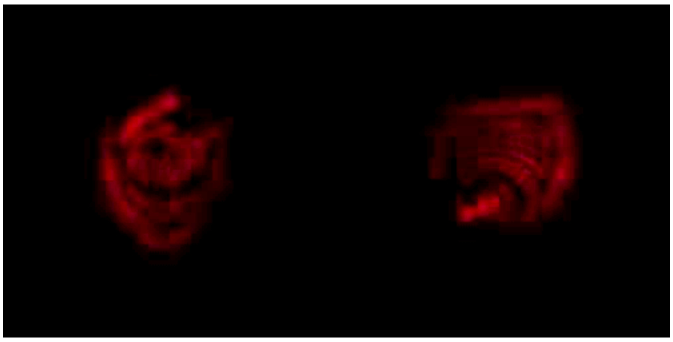

Figure 4.12: Out of focus images of the beam after the first iteration. On the left the image after the focus, on the right the image before the focus.

used a multiplicative constant equal to 0.3 and the final RMS error obtained with SH was 0.12339 *waves*, while with the curvature sensor it was 0.1210 *waves*. The comparison between the initial and the final wavefronts is shown in. The images in the focus of the telescope before and after the corrections are shown in Figure 4.15, and the cross section of a horizontal straight line passing for the centre is shown in Figure 4.16.

The graph of the coefficient k vs. the starting RMS error is shown in Figure 4.17. We have therefore proved that with our algorithm we were able to correct the multi-actuator lens with curvature sensing in order to eliminate aberrations.

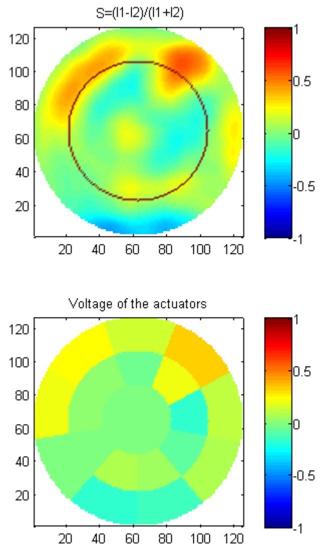

Figure 4.13: Comparison between the initial image and the final image on the focus of the telescope.

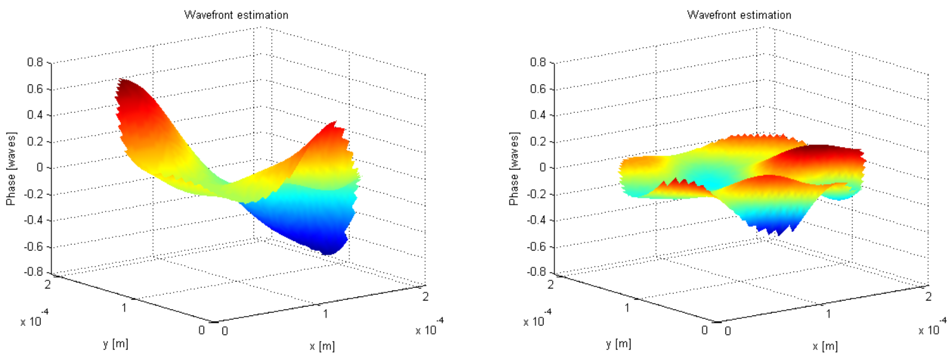

(a) (b)

Figure 4.14: Comparison of the initial (left) and final (right) wavefronts. Images obtained with the wavefront curvature sensor.

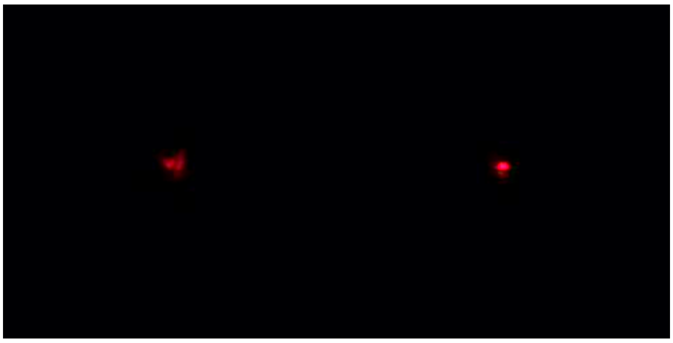

Figure 4.15: Comparison between the initial image and the final image on the focus of the telescope.

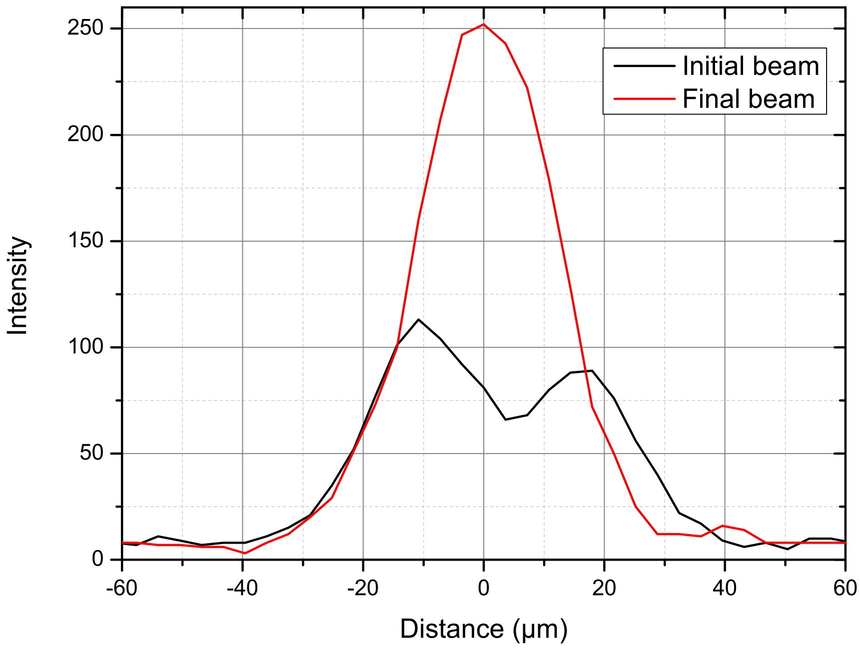

Figure 4.16: Cross section of the initial beam and the final beam.

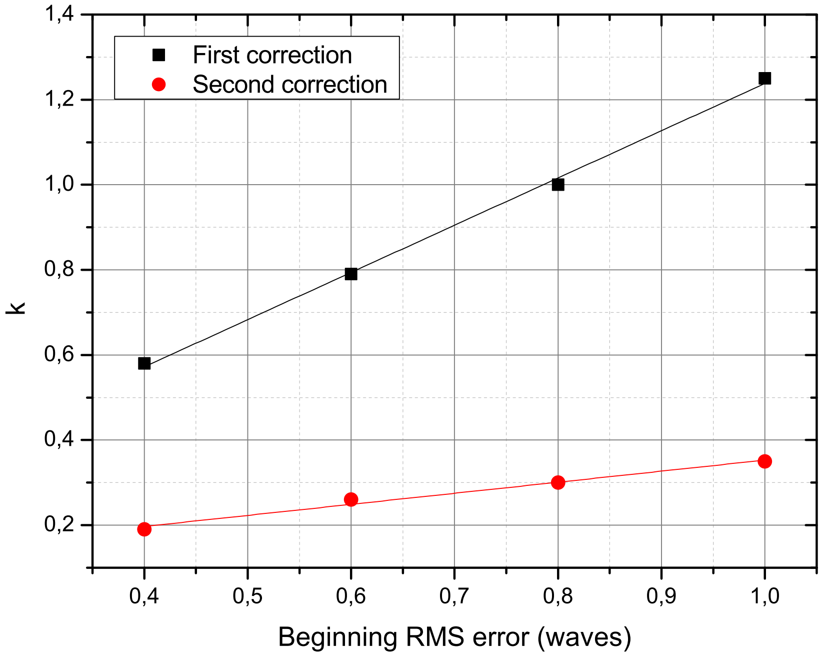

Figure 4.17: Graph of the coefficient vs the beginning RMS. The black linear trend is of the form $y = 0,128 + 1,11x$, while the red linear trend is of the form $y = 0,093 + 0,26x$.

Chapter 5

Fluorescence Microscopy and Depth Reconstruction

5.1 Fluorescence

When a molecule or an atom is hit by photons, it reaches an excitation state before emitting photons in turn with lower energy. This process is known as fluorescence (see Figure 5.1). In microscopy it usually occurs that a sample under study is be not fluorescent. Therefore a substance called fluorophore is bounded to the molecules of the sample with a particular chemical process to enable the fluorescence. Fluorescence microscopy uses photons to excite the fluorophore into a vibrational energy level. The fluorophore then rapidly relaxes to the lowest level

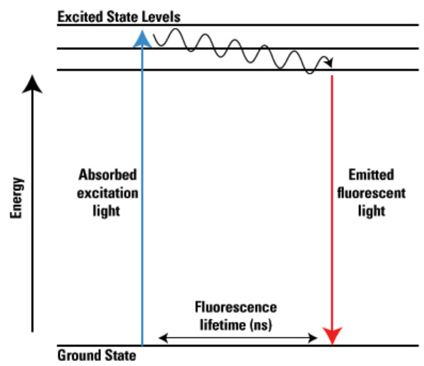

Figure 5.1: Scheme of the process of fluorescence.

of the excited state, with a process called internal conversion. At this point the molecule may dwell in the lowest excited state for $10^{-9}s$ and then can emit a photon to relax to the ground state. We can define the excitation rate as the product of the absorption cross section and the photon flux density,

$$k_{exc} = \sigma \Phi_{exc} = \frac{\sigma I_{exc}}{h\nu_{exc}}, \tag{5.1}$$

where σ is the cross section of the molecule, I_{exc} the excitation irradiance and $h\nu_{exc}$ the energy of the photon. k_{exc} is in unit of s^{-1}.
If we call n_0 the normalised population in the ground state S_0 and the normalised population n_1 in the excited state S_1, we have the following relation:

$$n_0 + n_1 = 1, \tag{5.2}$$

since the molecule can reside either in S_0 or in S_1.

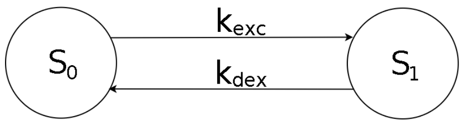

Figure 5.2: Ground state and excited population and corresponding rates.

The rate equation will be of the form

$$\frac{dn_0}{dt} = -k_{exc}n_0 + k_{dex}n_1, \tag{5.3}$$

where k_{dex} is the de-excitation rate from the excited state to the ground state. This rate is given by the sum of the spontaneous fluorescence emission rate and the non-fluorescent emission rate,: $k_{dex} = k_f + k_{nf}$.

At equilibrium the rate is null, thus we can write

$$0 = -k_{exc}n_0^{eq} + k_{dex}n_1^{eq}, \tag{5.4}$$

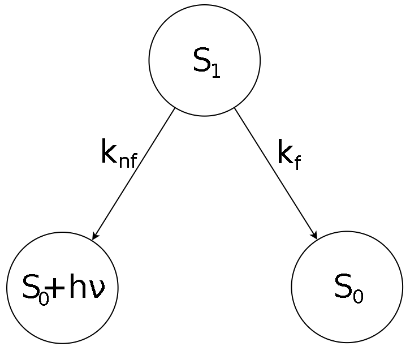

Figure 5.3: Fluorescent and-non fluorescent components of k_{dex}.

where the superscript eq indicates the equilibrium population. Equation 5.2 is still valid, thus we can write Equation 5.4 as

$$-k_{exc}n_0^{eq} + k_{dex}(1 - n_0^{eq}) = 0, \tag{5.5}$$

which leads to

$$n_0^{eq} = \frac{k_{dex}}{k_{exc} + k_{dex}}. \tag{5.6}$$

In abscence of excitation's photons, all molecules reside in the ground state.
If a brief light pulse excitates the system, the rate equation for the excited population just after the excitation (k_{exc}) will be

$$\frac{dn_1}{dt} = -\frac{dn_0}{dt} = 0 \cdot n_0 - k_{dex}n_1, \tag{5.7}$$

and the equation that we obtain is the well known decay law,

$$n_1(t) = n_1(0)e^{-\frac{t}{\tau}}, \tag{5.8}$$

where τ is the excited state lifetime and can be written as

$$\tau = \frac{1}{k_{dex}} = \frac{1}{k_f + k_{nf}}. \tag{5.9}$$

If we irradiate the total population and the rate of de-excitation is the same of the rate of excitation ($k_{exc} = k_{dex}$), the corresponding irradiance is known as saturation irradiance:

$$I_{sat} = \frac{h\nu_{exc}k_{dex}}{\sigma}. \tag{5.10}$$

5.2 Fluorescence microscopy

The basic function of a fluorescence microscope is to irradiate the specimen with a specific band of wavelengths, then to separate the fluorescence from the excitation light and finally to show to the user only the fluorescent light. Separation of excitation from emission is usually performed by filters and dichromatic mirrors. In fact, due to internal conversion, the energy of the fluorescence photons is less than the excitation photons, so the wavelength is red-shifted and the corresponding photons can be separated.

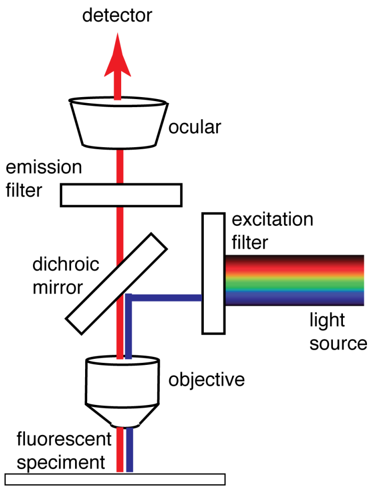

Figure 5.4: Operating diagram of a fluorescence microscope.

It can be demonstrated that the lateral resolution of a fluorescence microscope is

$$\delta r_{min} = \frac{0.61\lambda}{NA}, \tag{5.11}$$

where λ is the emission wavelength in vacuum and NA the numerical aperture of the microscope, while the axial resolution is

$$\delta z_{min} = \frac{2\lambda n}{NA^2}, \tag{5.12}$$

where n is the refractive index of the medium.

5.3 Total internal reflection fluorescence microscopy

This kind of microscopy uses the phenomenon of total internal reflection. The behaviour of the light between two mediums of refractive indices n_1 and n_2 is governed by the Snell's law

$$n_1 \sin(\theta_1) = n_2 \sin(\theta_2), \tag{5.13}$$

where θ_1 and θ_2 are the angles of the incident beam with respect to the normal to the interface. If n_1 is the lower refractive index and n_2 is the higher refractive index, then, when the light strikes the interface of the two materials at a sufficient high angle, the refraction direction is parallel to the interface. At the critical incidence angle, the Snell's law reduces to

$$n_1 \sin(\theta_c) = n_2. \tag{5.14}$$

Therefore, the critical angle is

$$\theta_c = \arcsin\left(\frac{n_2}{n_1}\right). \tag{5.15}$$

In the medium with refractive index n_2 there is a small amount of penetration of the light, which then propagates in parallel to the interface, creating an electromagnetic field. This field is said to be evanescent and within a region near the interface, it is capable of exciting fluorophores. The depth penetration of the evanescent wave is an exponential decay

$$E(z) = E(0)\ e^{-\frac{z}{d}}, \tag{5.16}$$

where z is the depth, normal to the interface and d is the penetration depth. Typically the evanescent wave can excite fluorophores restricted to a region that is less than 100 nm in thickness.

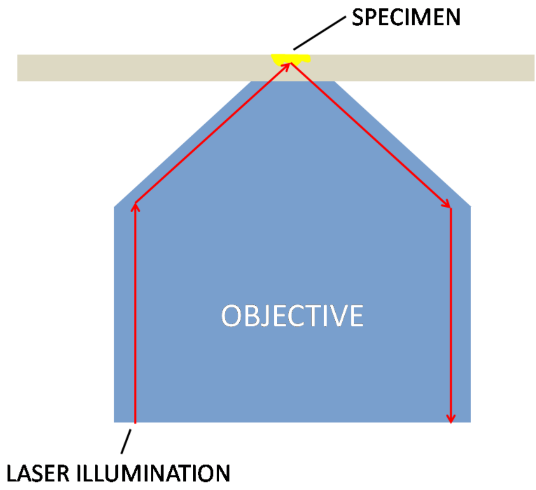

Figure 5.5: Scheme of the laser illumination on total internal reflection microscopy (TIRFM).

Generally, total internal reflection is implemented in a microscope with the objective lens technique. In this method, a high numerical aperture objective is used to obtain light which is incident to the sample with an angle higher than the critical one.

5.4 Confocal microscopy

In wide field microscopy, the entire depth of the sample over a wide area is illuminated, resulting in weak contrast and axial blurring. This is due to the fact that out of focus objects produce unwanted light that is collected by the objective.
On the other hand, in confocal microscopy, every point of the sample is illuminated once at a time by using a pinhole. A collimated laser is focused into the pinhole. The objective acts as a condenser for the laser, projecting a demagnified image of the pinhole on the sample (diffraction-limited spot). The fluorescent light from the sample is then collected by the detector by using another pinhole in front of

it. In this kind of microscopy, the lateral resolution i given by

$$\delta r_{minconf} = 0.7\delta r_{min} = \frac{0.4\lambda}{NA}, \tag{5.17}$$

and the axial resolution is

$$\delta z_{minconf} = 0.7\delta z_{min} = \frac{1.4\lambda n}{NA^2}. \tag{5.18}$$

These latter are better than corresponding resolution of the fluorescence microscopy.

5.5 Single molecule microscopy

In 2006 Rust, Bates and Zhuang [18] have presented the stochastic optical reconstruction microscopy (STORM). This kind of microscopy can reach an imaging resolution of 20 nm with the use of a simple total internal reflection fluorescence microscope, low-power continuous lasers and a photoswitchable fluorophore. If a fluorophore can be switched from fluorescent to dark state with the use of red and green laser respectively, we can use pulsed laser to turn on and off few molecules per cycle and repeat this cycle more and more times. By using multiple imaging cycles, we can obtain several positions for a single fluorophore, and if we find the centroid of the set of positions it is possible to resolve objects up to 20 nm (super resolution)

Unfortunately, STORM does not allow to obtain a 3D image of the sample, since the stimulated fluorophores can be in the focal plane of the objective or out of it, so the only super resolved coordinates are the two in the focal plane, say x and y, while the z-coordinate is at the diffraction limit.

However, in 2008 Wang, Wang, Bates and Zhuang [25] have presented a method to obtain three dimensional super resolution with STORM. To reach such a result, they have mounted a weak cylindrical lens on a microscope to create two different focal planes for the x and y direction. In fact, if the fluorophore is in the average focal plane, it appears round, while if it is above or below the average focal plane, it appears stretched in the x or in the y direction (see Figure 5.7). The calibration has been made by fitting a gaussian waist function for the x and y dimension as a function of the depth z. Finally, they have used the calibrating curves to find the z-coordinate of fluorophores on a sample by using their x and y dimensions.

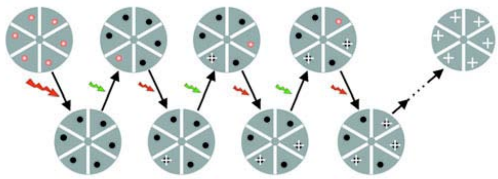

Figure 5.6: Sample labelled with red fluorophores that can be switched on and off with green and red. In each cycle the green laser is pulsed, so only a fraction emits fluorescence at the same time. Next, under red illumination, the molecules turn back to dark state, allowing their position (white crosses) to be determined. Finally multiple imaging cycles are repeated.

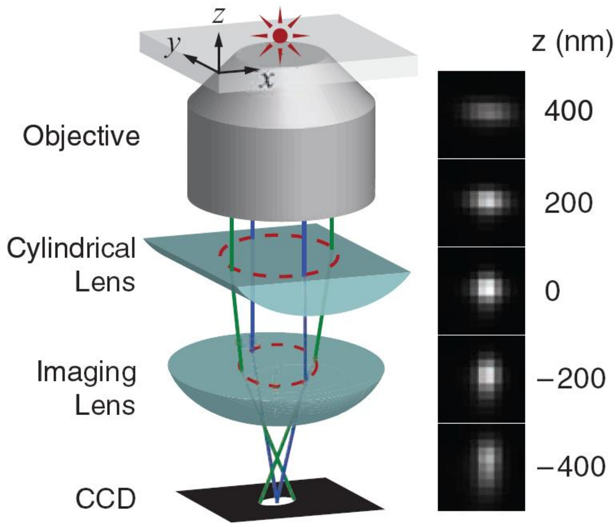

Figure 5.7: On the left, scheme of the three-dimensional STORM apparatus. On the right, change of shape of a fluorophore due to astigmatism at different depths.

5.6 Z-coordinate reconstruction with astigmatic wavefront on a microscope

In the last experiment, we have used the multi-actuator lens mounted on a fluorescence microscope. By using the lens with an astigmatic wavefront, we were able to reconstruct the depth (z-coordinate) of a specimen of quantum beads. This is only a preliminar experiment: in fact with fluorescence microscopy we could record a series of images at multiple depths and reconstruct the 3D image. However, this kind of analysis can be very useful in a future use of a single molecule microscope, because if we know how every molecule changes shape with astigmatism, with a single astigmatic image we could estimate the depth of every molecule in it.
The microscope used is schematised in Figure 5.8. The light emitted from a LED reflects at a dichroic mirror and passes through the objective lens before reaching the specimen. The fluorescence emitted from the specimen passes through the objective lens again and enters in a cooled 12 bit CCD camera, that captures the image and displayed it on the monitor of a computer.
The objective was an Olympus 60x with numerical aperture $NA = 1.35$. Over the objective it was mounted a piezoelectric actuator, Piezosystem Jena Mipos 100 driven by the Piezosystem Jena voltage amplifier 12V40, that was used for the z-scan. Finally, over the piezo actuator, it was mounted the multi-actuator lens. The LED which illuminated the sample was a blue high-power led (Thorlabs, M470L2) that emits light with nominal wavelength $\lambda = 470\ nm$ and a bandwidth (FWHM) $\Delta\lambda = 29\ nm$. The fluorescent sample used to test the algorithms was composed of some fluorescent quantum beads of diameter $15 - 20\ nm$ with excitation and emission wavelength compatible with our system. If we calculate the lateral resolution of the microscope with Equation 5.11, it is $226\ nm$, so the image of every quantum bead is the PSF of the microscope. The experiment we performed was

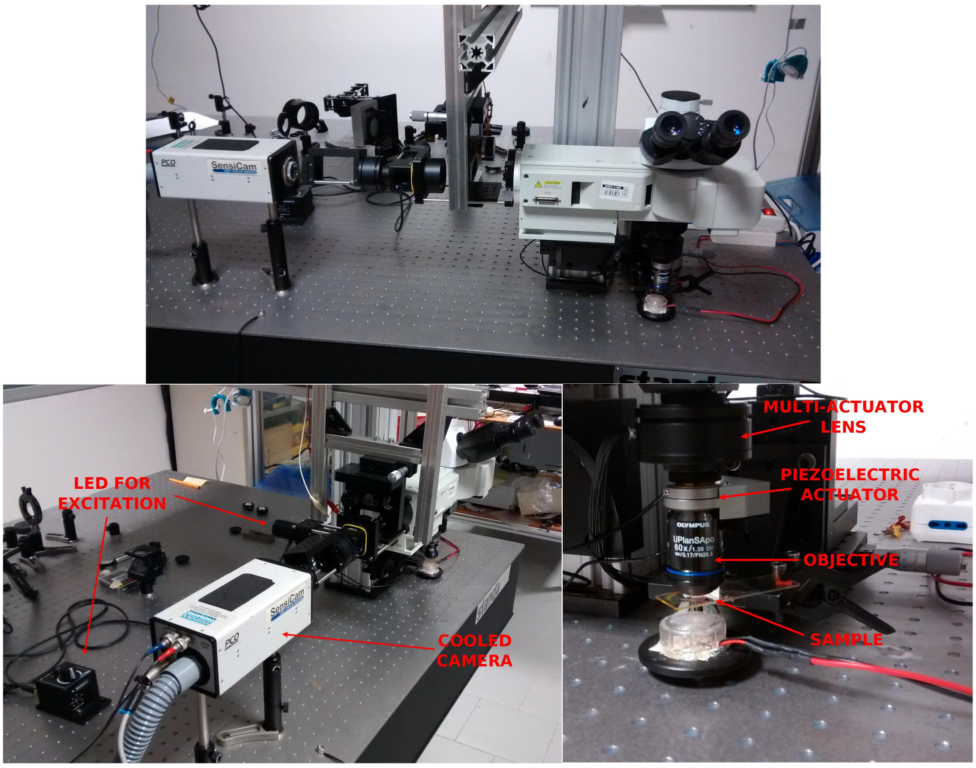

Figure 5.8: Images of the microscope used in the experiment.

about the reconstruction of the depth of a sample without taking a z-scan with the microscope. We used the multi-actuator lens with the quantum beads sample for the analysis of the depth reconstruction.

The first step was the use of the setup described in Chapter 3 to obtain a flat wavefront in closed loop. We saved the voltage values of the actuators. Once we obtained the flat wavefront we moved the lens on the microscope and set the voltage of the flat wavefront to the actuators. The next step was to add a small astigmatism to the lens to change the out of focus shape of the quantum beads. In fact, if we modify the flat wavefront with astigmatism, the out of focus images of the beads will be stretched more and more in the x dimension when we save multiple images in the positive z-direction over the focus of a bead. On contrast will be stretched more and more in the y dimension when we save multiple images in the negative z-direction with respect to the focus of the bead. In the focus the bead will appear as almost round. We measured the x and y dimension and plot these dimensions vs. the z-coordinate, see Figure 5.9.

The tendency of the lines is given by the waist of a gaussian beam, that is

$$w = w_0 \sqrt{1 + \frac{\lambda(z - z_0)}{\pi w_0^2} + \left[\frac{\lambda(z - z_0)}{\pi w_0^2}\right]^2 + A\left[\frac{\lambda(z - z_0)}{\pi w_0^2}\right]^3 + B\left[\frac{\lambda(z - z_0)}{\pi w_0^2}\right]^4}, \tag{5.19}$$

where λ is the wavelength, z_0 the z coordinate of the minimum dimension of the bead and w_0 the width of the bead when it is on focus. We used this formula to fit the data twice, once with the x dimension and once with the y dimension. Therefore we obtained the constants A and B.

Successively, we used the same sample, the quantum beads, for the analysis of the depth reconstruction. We chose a portion with some beads and took an image with astigmatic wavefront. We used an algorithm written in MATLAB to recognise the saturated signal and the x and y dimension of the non saturated beads. With

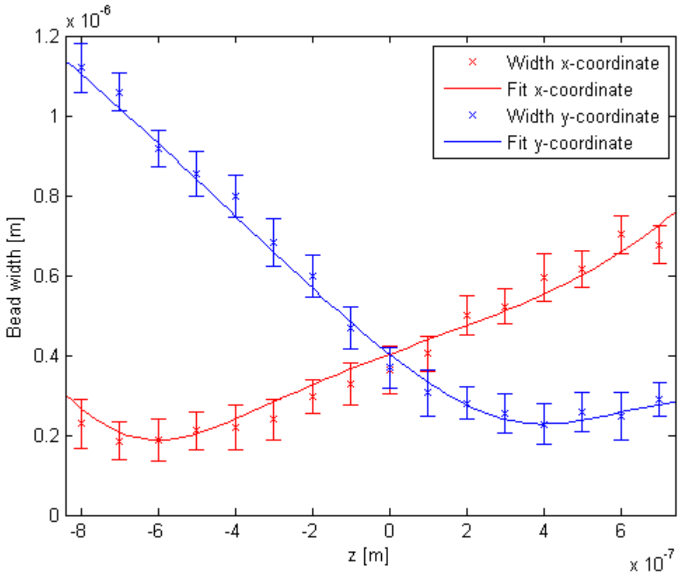

Figure 5.9: Fit of the x and y waist with function in Equation 5.19.

this information we extrapolated the z value by using Equation 5.19. After the estimation of the z coordinate for every involved bead, we verified the obtained values with the real analysis of the position of the beads, by making a z-stack of the sample with the piezoelectric actuator.

For example, the xy image obtained with the astigmatic wavefront is in Figure 5.10. In the image the bead on the bottom left is saturated (values equal to $2^{12} - 1$), so it had not been analysed. Instead the other beads were below the threshold of the software recognition. After the analysis, the xy image is that shown in Figure 5.11, and the three dimensional image is in Figure 5.12.

We used the piezoelectric z-stack actuator with step of z-coordinate of 0.1 μm to obtain multiple images with flat wavefront at several depth of the sample. We then compared them with the astigmatic method just presented. Once we obtained the images, we took the same quantum beads and plotted the average value of the intensity of the bead vs the z-coordinate. The figure obtained was fitted with a gaussian function and the z-coordinate in correspondence of the maximum value

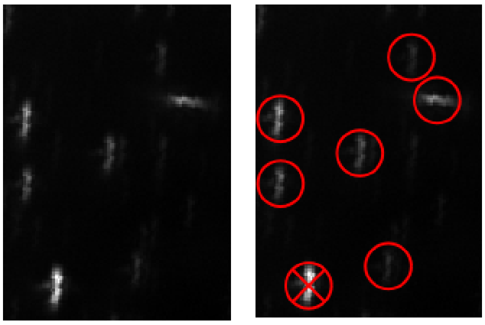

(a) (b)

Figure 5.10: Portion of quantum beads with astigmatic wavefront. On the left the original image, on the right the selected beads and the saturated bead.

was taken as the centre of the bead. The zero z-coordinate in the astigmatic case was given by the centre of the beads used for the fit of the waist. Instead in the scan with the piezoelectric actuator, the zero z-coordinate was chosen for the first image. Consequently, the second image had z-coordinate of 0.1 μm and so on.

To compare the two different results we subtracted the minimum z-coordinate to the others, see Figure 5.13. The residual of the z coordinate for every bead is shown in Figure 5.14. The maximum difference resulted to be 45 nm and the posterior error given by the fit of the waist was 36 nm, instead we obtained a mean σ equal to 95 nm by the gaussian fit. We then concluded that the z reconstruction with astigmatism has given a good estimation of the z-coordinate. Another depth analysis in a different region of the sample is shown in Figures 5.15, 5.16 and 5.17. Other analyses have been made in other regions with the same sample of quantum beads, and the residuals of the two methods have always been less than 60 nm. Moreover, the uncertainty on the z-coordinate with astigmatic wavefront has always been lower than the one obtained with the scan with the piezoelectric actuator.

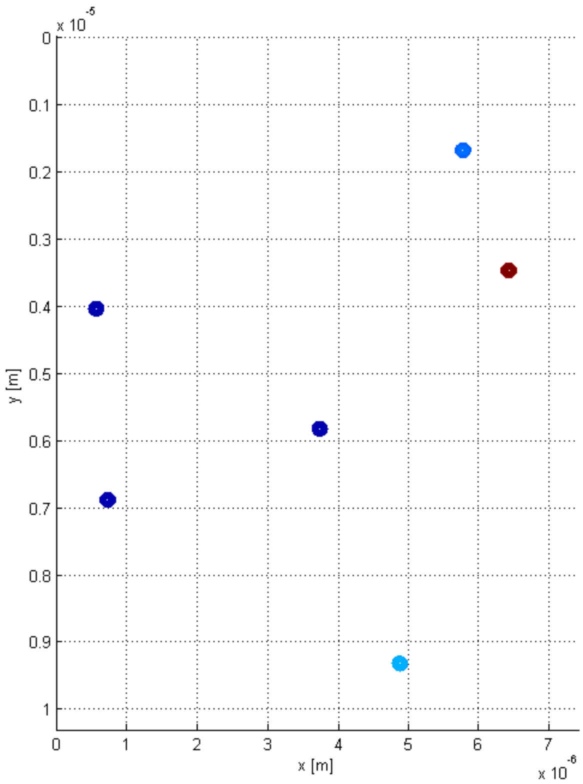

Figure 5.11: Graph of the xy-reconstruction with astigmatic wavefront. With the piezoelectric scan we have obtained the same xy-coordinates.

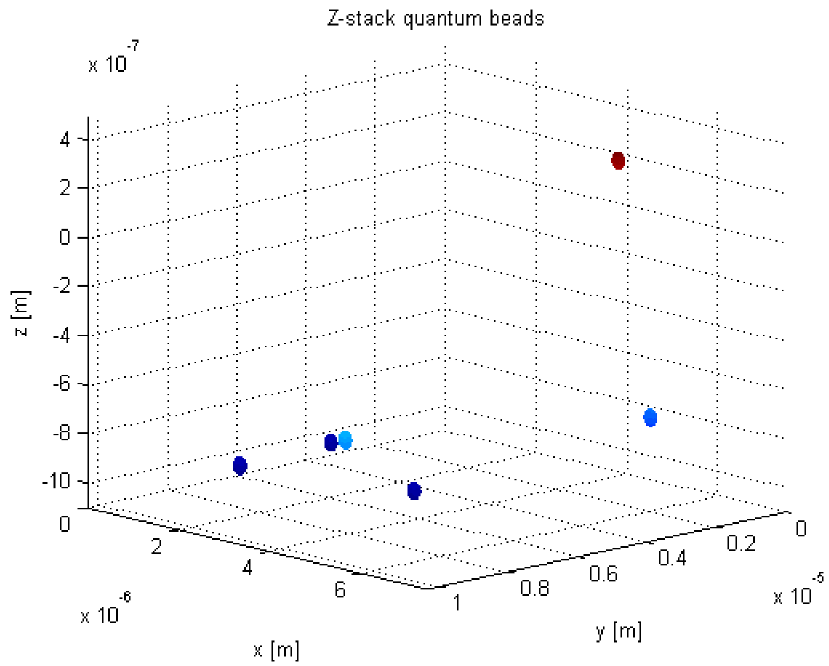

Figure 5.12: Graph of the xyz-reconstruction with astigmatic wavefront.

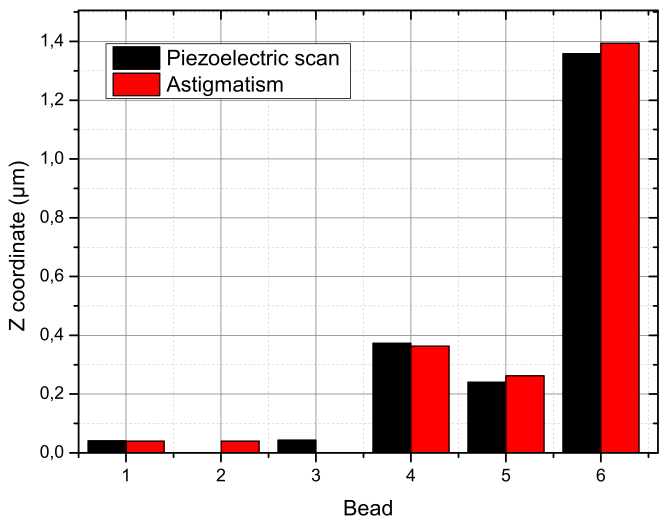

Figure 5.13: Comparison of the z-coordinate of the two methods.

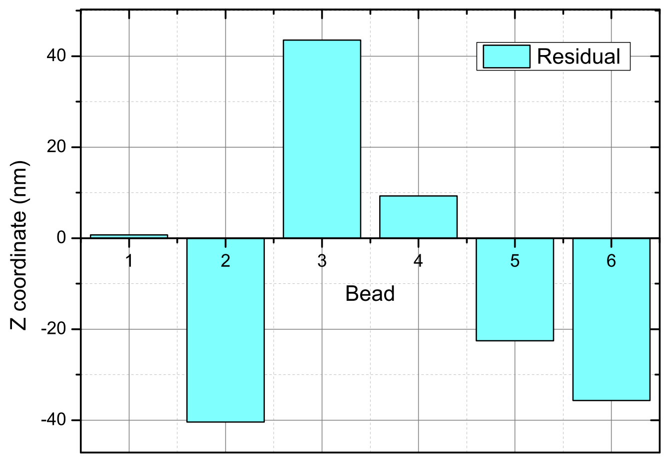

Figure 5.14: Residual of the z-coordinate obtained with the two methods. Note that in this case the scale of the z-coordinate is in nanometres.

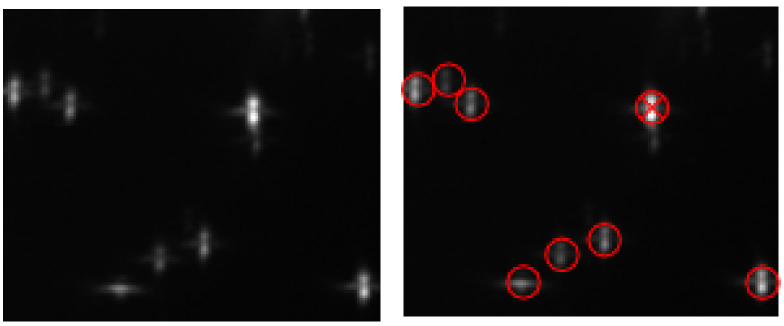

(a) (b)

Figure 5.15: Portion of quantum beads with astigmatic wavefront. On the left the original image, on the right the selected beads and the saturated bead.

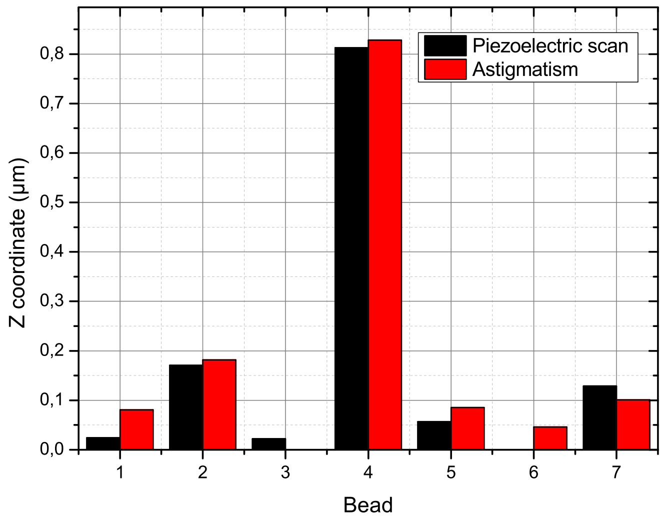

Figure 5.16: Comparison of the z coordinate of the two methods.

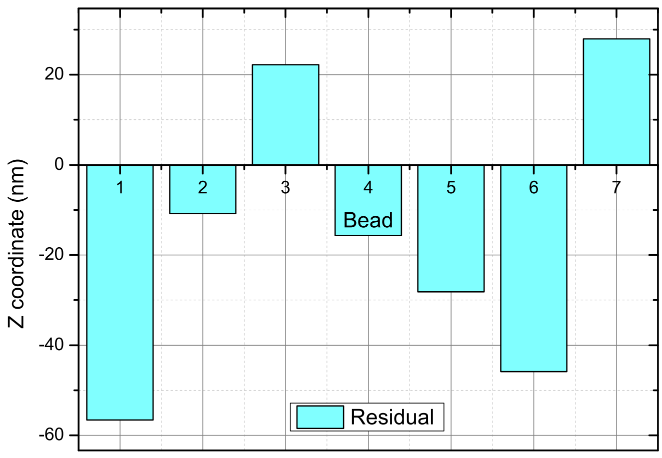

Figure 5.17: Residual of the z coordinate obtained with the two methods. Note that in this case the scale of the z coordinate is in nanometres.

Conclusions

In this thesis we have implemented a wavefront curvature sensor, we have used a multi-actuator lens to correct a wavefront by using curvature sensing and we have used the multi-actuator lens mounted on a microscope to reconstruct a three dimensional image by using a single image on an xy plane with astigmatic wavefront.

The wavefront curvature sensor has presented good linearity up to Zernike coefficients of 1 *waves*. However, the spectral purity of the sensor could be improved with a couple of modifications to the setup. In fact, the recorded out of focus images presented a non negligible noise and sometimes there was diffraction caused by the laser. A possible improvement can be obtained with a more sensitive sensor and with a not coherent source.

The wavefront curvature control has shown that with out of focus images it is possible to drive the multi-actuator lens in order to obtain an almost flat wavefront. However, this kind of control has not allowed us to get a flat wavefront that satisfied the Marèchal criterion, thus in this case the change of the sensor and of the source could let us to satisfy the criterion.

Finally, the z-coordinate reconstruction with the astigmatic wavefront has shown that the multi-actuator lens can be used for the creation of 3D images. Moreover, in our setup there is no need to modify the system by adding an astigmatic lens as in the experiment of Zhuang, because the multi-actuator lens can be used to

obtain all the aberrations up to the fourth order of the Zernike polynomials.
The last experiment with the fluorescence microscope can be easily translated to a single molecule microscope in the future and the multi-actuator lens could avoid the modification of the system.

Appendix A

Irradiance Transport Equation

Here we present the derivation of the irraddiance transport equation [21].

Assume that a paraxial beam is propagating along the z axis, and let us compute the complex amplitude

$$u_z(\vec{r}) = \sqrt{I_z(\vec{r})}e^{ikW_z(\vec{r})} = sqrtI_z(\vec{r})e^{i\Phi_z(\vec{r})}, \tag{A.1}$$

where $r = (x, y)$ is the radial coordinate orthogonal to the propagation direction, $I_z(\vec{r})$ is the irradiance, $k = 2\pi/\lambda$ the wavenumber and $W_z(\vec{r})$ the phase $\Phi_z(\vec{r})$ in terms of the wavelength λ. The time-independent wave equation in empty space can be written as

$$\Big[\frac{\partial^2}{\partial z^2} + \nabla^2 + k^2\Big]\psi_z(\vec{r}) = 0, \tag{A.2}$$

where $\nabla^2 = \partial_x^2 + \partial_y^2$ and $\psi_z(\vec{r})$ an auxiliary function. Another way to write the same equation is by introducing the two operators

$$L_\pm = \frac{\partial}{\partial z} \mp \imath k\Big[1 + \Big(\frac{\nabla}{k}\Big)^2\Big]^{1/2}. \tag{A.3}$$

Therefore the time-independent wave equation becomes

$$L_+L_-\psi_z(\vec{r}) = 0. \tag{A.4}$$

The solution of Equation A.2 thus separate into two classes:

$$L_+u_z(\vec{r}) \tag{A.5}$$

and

$$L_{-}v_z(\vec{r}) \tag{A.6}$$

. The solutions u_z describe either oscillatory waves with a positive z component of the wave vector $2\pi[r, (1/\lambda)(1-\lambda^2 r^2)^{1/2}]$ or evanescent waves if $\lambda^2 r^2 > 1$ and $z > 0$, whereas the solutions v_z describe either oscillatory waves with a negative z of the wave vector $2\pi[r, -(1/\lambda)(1-\lambda^2 r^2)^{1/2}]$ or evanescent waves if $\lambda^2 r^2 > 1$ and $z < 0$. In the abscence of scattering by charge matter, the solutions does not mix. Hereafter, we consider only the solutions u_z.
A formal solution of Equation A.5 may be written as

$$u_z(\vec{r}) = u_0(\vec{r}) e^{ikz\left(1+\frac{\nabla^2}{k^2}\right)^{1/2}}. \tag{A.7}$$

The square-root operator is defined in terms of the Fourier transform of Equation A.7:

$$U_z(\rho) = U_0(\rho) e^{ikz(1-\lambda^2\rho^2)^{1/2}} = \int dr e^{-i2\pi\rho\cdot r} u_z(\vec{r}) = \mathcal{F}\{u_z(\vec{r})\}. \tag{A.8}$$

The inverse Fourier transform relationship is

$$\mathcal{F}^{-1}\{e^{ikz(1-\lambda^2\rho^2)^{1/2}}\} = -\frac{1}{2\pi}\frac{\partial}{\partial z}\frac{e^{ikR}}{R}, \tag{A.9}$$

where $R = (z^2 + r^2)^{1/2}$. Therefore, from Equations A.8 and A.9 we have

$$u_z(\vec{r}) = -\frac{1}{2\pi}\frac{\partial}{\partial z}\Big[u_0(\vec{r}) * \frac{e^{ikR}}{R}\Big], \tag{A.10}$$

which is the Rayleigh-Sommerfeld diffraction theory, that gives the wave amplitude in a transverse plane $z \geq 0$ in terms of the wave plane in an earlier plane $z = 0$. Notice that $*$ denotes the two dimensional convolution, that for two functions f and g is

$$f(\vec{r}) * g(\vec{r}) = \int dr' f(r') g(r - r'). \tag{A.11}$$

The conventional Fresnel diffraction theory results when the square roots in Equations A.7 and A.8 are expanded to the lowest order to get

$$u_z(\vec{r}) = u_0(\vec{r})e^{ikz}e^{i\frac{\lambda z \nabla^2}{4\pi}} \tag{A.12}$$

and

$$U_z(\rho) = U_0(\vec{r})e^{ikz}e^{-i\pi\lambda z\rho^2} \tag{A.13}$$

and, using the inverse Fourier transform relationship,

$$\mathcal{F}^{-1}\{e^{-i\pi\lambda z\rho^2}\} = \frac{e^{i\pi r^2/\lambda z}}{i\lambda z}, \tag{A.14}$$

we have from Equation A.12

$$u_z(\vec{r}) = e^{ikz}\left[u_0(\vec{r}) * \frac{e^{i\frac{\pi r^2}{\lambda z}}}{i\lambda z}\right], \tag{A.15}$$

which is the Fresnel diffraction theory result.

We can take Equation A.15 and verify that it solves the parabolic equation, that is

$$\left(i\frac{\partial}{\partial z} + \frac{\nabla^2}{2k} + k\right)u_z(\vec{r}) = 0. \tag{A.16}$$

If we now multiply Equation A.16 on the left-hand side by $u_z^*(\vec{r})$ and the complex conjugate by $u_z(\vec{r})$ on the left-hand side and subtract them, we get

$$u_z^*(\vec{r})\left(i\frac{\partial}{\partial z} + \frac{\nabla^2}{2k} + k\right)u_z(\vec{r}) - u_z(\vec{r})\left(-i\frac{\partial}{\partial z} + \frac{\nabla^2}{2k} + k\right)u_z^*(\vec{r}) = 0. \tag{A.17}$$

Now we write the complex amplitude as in Equation A.1, $u_z(\vec{r}) = I_z^{1/2}(\vec{r})e^{i\Phi_z(\vec{r})}$, so Equation A.17 becomes

$$\begin{aligned} I_z^{1/2}(\vec{r})e^{-i\Phi_z(\vec{r})}\left(i\frac{\partial}{\partial z} + \frac{\nabla^2}{2k} + k\right)I_z^{1/2}(\vec{r})e^{i\Phi_z(\vec{r})} + \\ -I_z^{1/2}(\vec{r})e^{i\Phi_z(\vec{r})}\left(-i\frac{\partial}{\partial z} + \frac{\nabla^2}{2k} + k\right)I_z^{1/2}(\vec{r})e^{-i\Phi_z(\vec{r})} = 0. \end{aligned} \tag{A.18}$$

If we develop the above equation we get

$$\begin{aligned} iI_z^{1/2}(\vec{r})\frac{\partial}{\partial z}\big[I_z^{1/2}(\vec{r})\big]+ \\ &+ iI_z(\vec{r})e^{-i\Phi_z(\vec{r})}\frac{\partial}{\partial z}\big[e^{i\Phi_z(\vec{r})}\big]+ \\ &+ I_z^{1/2}(\vec{r})\frac{\nabla^2}{2k}\big[I_z^{1/2}(\vec{r})\big]+ \\ &+ I_z(\vec{r})e^{-i\Phi_z(\vec{r})}\frac{\nabla^2}{2k}\big[e^{+i\Phi_z(\vec{r})}\big]+ \\ &+ \frac{I_z^{1/2}(\vec{r})e^{-i\Phi_z(\vec{r})}}{k}\big(\nabla I_z^{1/2}(\vec{r})\big)\cdot\big(\nabla e^{i\Phi_z(\vec{r})}\big)+ \\ &+ iI_z^{1/2}(\vec{r})\frac{\partial}{\partial z}\big[I_z^{1/2}(\vec{r})\big]+ \\ &+ iI_z(\vec{r})e^{i\Phi_z(\vec{r})}\frac{\partial}{\partial z}\big[e^{-i\Phi_z(\vec{r})}\big]+ \\ &- I_z^{1/2}(\vec{r})\frac{\nabla^2}{2k}\big[I_z^{1/2}(\vec{r})\big]+ \\ &- I_z(\vec{r})e^{i\Phi_z(\vec{r})}\frac{\nabla^2}{2k}\big[e^{-i\Phi_z(\vec{r})}\big]+ \\ &- \frac{I_z^{1/2}(\vec{r})e^{i\Phi_z(\vec{r})}}{k}\big(\nabla I_z^{1/2}(\vec{r})\big)\cdot\big(\nabla e^{-i\Phi_z(\vec{r})}\big). \end{aligned} \tag{A.19}$$

We resort to the following equations

$$\nabla\big(I_z^{1/2}(\vec{r})\big) = \frac{\nabla I_z(\vec{r})}{2I_z^{1/2}(\vec{r})} \tag{A.20}$$

$$\nabla e^{i\Phi_z(\vec{r})} = i\nabla\Phi_z(\vec{r})e^{i\Phi_z(\vec{r})} \tag{A.21}$$

$$\nabla e^{-i\Phi_z(\vec{r})} = -i\nabla\Phi_z(\vec{r})e^{-i\Phi_z(\vec{r})} \tag{A.22}$$

$$\nabla^2\big(I_z^{1/2}(\vec{r})\big) = \frac{\big(\nabla I_z(\vec{r})\big)^2}{2I_z^{3/2}(\vec{r})} + \frac{\nabla^2 I_z(\vec{r})}{2I_z^{1/2}(\vec{r})} \tag{A.23}$$

$$\nabla^2 e^{i\Phi_z(\vec{r})} = i\nabla^2\Phi_z(\vec{r})e^{i\Phi_z(\vec{r})} - \big(\nabla\Phi_z(\vec{r})\big)^2 e^{i\Phi_z(\vec{r})} \tag{A.24}$$

$$\nabla^2 e^{-i\Phi_z(\vec{r})} = -i\nabla^2\Phi_z(\vec{r})e^{-i\Phi_z(\vec{r})} - \big(\nabla\Phi_z(\vec{r})\big)^2 e^{-i\Phi_z(\vec{r})} \tag{A.25}$$

to write Equation A.19 as follows:

$$\frac{i}{2}\frac{\partial I_z(\vec{r})}{\partial z} - I_z(\vec{r})\frac{\partial \Phi_z(\vec{r})}{\partial z} + \frac{I_z^{1/2}(\vec{r})}{2k}\left[\frac{\big(\nabla I_z(\vec{r})\big)^2}{2I_z^{3/2}(\vec{r})} + \frac{\nabla^2 I_z(\vec{r})}{2I_z^{1/2}(\vec{r})}\right] +$$
$$+ \frac{I_z(\vec{r})e^{-i\Phi_z(\vec{r})}}{2k}\left[i\nabla^2\Phi_z(\vec{r})e^{i\Phi_z(\vec{r})} - \big(\nabla\Phi_z(\vec{r})\big)^2 e^{i\Phi_z(\vec{r})}\right] + \frac{i}{2k}\big(\nabla I_z(\vec{r})\big)\cdot\big(\nabla\Phi_z(\vec{r})\big)+$$
$$+ \frac{i}{2}\frac{\partial I_z(\vec{r})}{\partial z} + I_z(\vec{r})\frac{\partial \Phi_z(\vec{r})}{\partial z} - \frac{I_z^{1/2}(\vec{r})}{2k}\left[\frac{\big(\nabla I_z(\vec{r})\big)^2}{2I_z^{3/2}(\vec{r})} + \frac{\nabla^2 I_z(\vec{r})}{2I_z^{1/2}(\vec{r})}\right] +$$
$$- \frac{I_z(\vec{r})e^{i\Phi_z(\vec{r})}}{2k}\left[-i\nabla^2\Phi_z(\vec{r})e^{-i\Phi_z(\vec{r})} - \big(\nabla\Phi_z(\vec{r})\big)^2 e^{-i\Phi_z(\vec{r})}\right] +$$
$$+ \frac{i}{2k}\big(\nabla I_z(\vec{r})\big)\cdot\big(\nabla\Phi_z(\vec{r})\big) = 0. \tag{A.26}$$

If we develop the above equation we obtain

$$i\frac{\partial I_z(\vec{r})}{\partial z} + \frac{I_z(\vec{r})}{2k}\big[i\nabla^2\Phi_z(\vec{r}) - \big(\nabla\Phi_z(\vec{r})\big)^2\big] + \frac{i}{2k}\big(\nabla I_z(\vec{r})\big)\cdot\big(\nabla\Phi_z(\vec{r})\big)+$$
$$-\frac{I_z(\vec{r})}{2k}\big[-i\nabla^2\Phi_z(\vec{r}) - \big(\nabla\Phi_z(\vec{r})\big)^2\big] + fraci2k\big(\nabla I_z(\vec{r})\big)\cdot\big(\nabla\Phi_z(\vec{r})\big) = 0. \tag{A.27}$$

Finally, the result of the previous equation is

$$k\frac{\partial I_z(\vec{r})}{\partial z} + I_z(\vec{r})\nabla^2\Phi_z(\vec{r}) + \big(\nabla I_z(\vec{r})\big)\cdot\big(\nabla\Phi_z(\vec{r})\big) = 0, \tag{A.28}$$

and if we substitute the phase with $W_z(\vec{r}) = \Phi_z(\vec{r})/k$ we obtain

$$\frac{\partial I_z(\vec{r})}{\partial z} + I_z(\vec{r})\nabla^2 W_z(\vec{r}) + \big(\nabla I_z(\vec{r})\big)\cdot\big(\nabla W_z(\vec{r})\big) = 0, \tag{A.29}$$

that is the irradiance transport equation given in Chapter 2.

Appendix B

Matlab Codes

Code B.1: Algorithm of the wavefront curvature sensor.

```
function Wavefront=CalculateWavefront(I1tmp,I2tmp,...
        centerI1tmp,centerI2tmp,halfdim,...
                f,l,influencematrix,angle,cut)

  % cut the images if it is necessary
  if(cut==1)
        I1tmp=CutImage(I1tmp,centerI1tmp(1),...
                centerI1tmp(2),halfdim);
        I2tmp=CutImage(I2tmp,centerI2tmp(1),...
                centerI2tmp(2),halfdim);
  end
  aperturelens=10e-3; %metre
  dimpixel=3.6e-6; %metre
  deltaz=f*(f-l)/(2*l);
  zernikeModes=66;

  % Calculate the mask to use
  mask=CalculateMaskGeometrically(f,l,...
                aperturelens,dimpixel);

  center=floor(size(I1tmp,1)/2);
  diameterx=size(mask,1);
  diametery=size(mask,1);
  left=floor(center-diameterx/2);
  up=floor(center-diametery/2);

  fourierDim=size(mask,1);
```

```

aperturePixelSize=(dimpixel*f)/l;

if(mod(size(mask,1),2)==0)
  up=up+1;
  left=left+1;
end

I1=I1tmp(left:left+diameterx-1,up:up+diametery-1);
I2=I2tmp(left:left+diameterx-1,up:up+diametery-1);
I2=imrotate(I2,180);

% Plot the images cut with the mask
I1plot=I1.*mask;
I1plot(mask==0)=nan;
figure,pcolor(I1plot), shading interp,..
        title('Image after focus cut')
I2plot=I2.*mask;
I2plot(mask==0)=nan;
figure,pcolor(I2plot), shading interp,...
    title('Image before focus cut')

% Find the indices of nonzero elements
ApIdx = find(mask);

% Find the indices of zero elements
outIdx = find(~mask);

% Find a ring in the border of the mask
ApringOut = xor(imdilate(mask,strel('disk',1)),mask);

ApringIn = xor(imerode(mask,strel('disk',1)),mask);

[borderx, bordery] = find(ApringIn);

% Calculus of spatial frequencies for FFT
[u, v] = meshgrid( (-0.5:1/fourierDim:0.5-1/fourierDim)/...
aperturePixelSize);
u2v2 = -4*pi^2*(u.*u + v.*v);
center=floor(fourierDim/2+1);
u2v2(center,center) = Inf;
iu2v2=u2v2;
iu2v2(center,center) = 0;
```

```
% Creation of the signal S1 = -1/deltaz*(I1-I2)./(I1+I2)
num=diameterx-1;
x2 = -1:2/num:1;
[X,Y] = meshgrid(x2,x2);
[theta,r] = cart2pol(X,Y);
Sin=-1/deltaz*(I1-I2)./(I1+I2);
Sin(isnan(Sin))=0;
S=Sin;

% Z contains the Zernike polynomials
Z=sh_zernikeR_all(X,Y);

%set the maximum number of iterations
iterations=20;

RMSerror=zeros(iterations,1);
coeff=zeros(zernikeModes,iterations);
Wrms=zeros(fourierDim,fourierDim,iterations);
Wfinal=zeros(fourierDim,fourierDim,iterations);
stop=0;

jj=1;

while jj<=iterations && stop==0
  % Calculus of the wavefront using FFT
  SFFT = fftshift(fft2( fftshift(S) ));
  W = fftshift( ifft2( fftshift( SFFT./u2v2 )) );

  Wabs=real(W);

  Wfinal(:,:,jj)=Wabs;

  % Calculate Zernike coefficients
  coeff(:,jj)=ZernikeCoefficientsMask(zernikeModes,...
              mask,Wabs);
  Wtmp=Wabs;

  WestdWdn0=Wtmp;

  % 3x3 average in the border of the mask to set
  % the derivative of the wavefront zero on the border
```

```
    for ii = 1:length(borderx)
      reg = Wtmp(borderx(ii)-1:borderx(ii)+1,...
              bordery(ii)-1:bordery(ii)+1);
          intersectIdx = find(ApringIn(borderx(ii)-1...
                  :borderx(ii),bordery(ii)-1:bordery(ii)));
          WestdWdn0(borderx(ii),bordery(ii))=...
                  mean( reg(intersectIdx) );
    end

    Wt=WestdWdn0;

    %Calculate the signal by using discrete laplacian
    Wxx = zeros( fourierDim );
    Wyy = zeros( fourierDim );
    for kk=1:fourierDim
      for ll=2:fourierDim-1
        Wxx(kk,ll)=(Wt(kk,ll-1)-2*Wt(kk,ll)+Wt(kk,ll+1))/...
            (aperturePixelSize^2);
      end
    end
    for kk=2:fourierDim-1
      for ll=1:fourierDim
        Wyy(kk,ll)=(Wt(kk-1,ll)-2*Wt(kk,ll)+Wt(kk+1,ll))/...
                (aperturePixelSize^2);
      end
    end

    Sest = Wxx + Wyy;

    Wrms(:,:,jj)=Wt;

    % Calculate the RMS error
    RMSerror(jj)=sqrt(sum(sum((Sest.*mask-Sin.*mask).^2))/...
            (sum(sum(mask))));

    if(jj>1 && RMSerror(jj)>RMSerror(jj-1))
      stop=1;
    end

    Sest(ApIdx)=Sin(ApIdx);
    S=Sest;

    jj=jj+1
```

```
  end

  % Calculate the wavefront by using
  % the calculated coefficients
  coeff(:,jj-1)=nan;
  func=0;
  coeff(1:3,:)=0;
  for kk=1:66
    func=func+coeff(kk,jj-2)*Z(:,:,kk);
  end

  Wavefront=func;


  figure,pcolor(Wavefront.*mask),shading interp;

end
```

Code B.2: Algorithm of the wavefront curvature control.

```
function [Signal, actuatorvalue]=CalculateSignal(I1tmp,...
        I2tmp,centerI1tmp,centerI2tmp,halfdim,f,l,angle,...
        influencematrix)


  I1tmp=CutImage(I1tmp,centerI1tmp(1),centerI1tmp(2),...
          halfdim);
  I2tmp=CutImage(I2tmp,centerI2tmp(1),centerI2tmp(2),...
          halfdim);

  aperturelens=10e-3; %metre
  dimpixel=3.6e-6; %metre
  deltaz=1;

  % Calculate the mask of the actuators
  [mask,maskext,maskactuators,diameter]=...
    CalculateMaskActuators(f,l,aperturelens,dimpixel,angle);

  center=floor(size(I1tmp,1)/2);
  diameterx=diameter;
  diametery=diameter;
  left=floor(center-diameterx/2);
```

```
up=floor(center-diametery/2);

aperturePixelSize=dimpixel*f/(l);

if(mod(size(mask,1),2)==0)
  up=up+1;
  left=left+1;
end

% Create the signal S=-1/deltaz*(I1-I2)./(I1+I2)
I1=I1tmp(left:left+diameterx-1,up:up+diametery-1);
I2=I2tmp(left:left+diameterx-1,up:up+diametery-1);
I2=imrotate(I2,180);
S=-(I1-I2)./(I1+I2);

ApringIn = xor(imerode(mask,strel('disk',1)),mask);
Signal=S.*maskext;
Signal(ApringIn==1)=2;
Signal(maskext==0)=nan;
figure,subplot(2,1,1),pcolor(flipud(Signal)),...
        shading interp,title 'S=-(I1-I2)/(I1+I2)',...
        colorbar,caxis([-1,1]),axis equal tight;

Sactuators=S;
actuatorvalue=zeros(19,1);
for kk=1:19
  actuatorvalue(kk)=mean(mean(S(maskactuators==kk)));
  Sactuators(maskactuators==kk)=actuatorvalue(kk);
end

Sactuators(maskext==0)=nan;
subplot(2,1,2),pcolor(flipud(Sactuators)),...
        shading interp,title 'Voltage of the actuators',...
        colorbar,caxis([-1,1]),axis equal tight;
```

Code B.3: Algorithm of z-coordinate retrieval with astigmatic wavefront on a microscope.

```
% Data obtained by the fit
Ax=-0.261769;
Bx=0.0273014;
x0=-0.0000006;
w0x=1.87272E-07;
```

```
Ay=-0.41266;
By=-0.0629869;
y0=0.0000004;
w0y=2.27934E-07;

% Fix the noise of the image
noise=200;

% Calculate the waist in the x and y direction
x=linspace(-1e-6,1e-6,100);
wrowest= w0x*sqrt( 1+ ((500E-09*(x-x0))/(3.1415*w0x^2)).^2...
 + Ax*((500E-09*(x-x0))/(3.1415*w0x^2)).^3 +Bx*((500E-09*...
 (x-x0))/(3.1415*w0x^2)).^4 );
wcolest= w0y*sqrt( 1+ ((500E-09*(x-y0))/(3.1415*w0y^2)).^2...
 + Ay*((500E-09*(x-y0))/(3.1415*w0y^2)).^3 +By*((500E-09*...
 (x-y0))/(3.1415*w0y^2)).^4 );

% open the data of the points for the plot
fileIDx = fopen('fitxc.txt','r');
fileIDy = fopen('fityc.txt','r');
formatSpec='%f %f';
sizedata = [2 Inf];
datax= fscanf(fileIDx,formatSpec,sizedata);

% Error of the width and height of the files
errorx=load('Errorx','Errorx');
errory=load('Errory','Errory');

% Error of the fit
load('erry','erry')

datay=fscanf(fileIDy,formatSpec,sizedata);

% Plot the two waists and the points
figure, errorbar(datax(1,:),datax(2,:),errorx,'rx'), ...
  axis([-8.4e-7 7.4e-7 0 1.2e-6]),xlabel('z [m]'),...
  ylabel('Bead width [m]'),box on, hold on;
plot(x,wrowest,'r'),hold on;
errorbar(datay(1,:),datay(2,:),errory,'bx'),hold on;
plot(x,wcolest,'b');
legend('Width x-coordinate','Fit x-coordinate',...
  'Width y-coordinate','Fit y-coordinate')
```

```

% Read the image to analyse
image=imread('image36.png');
image=imrotate(image,10,'crop');
cutim=image(670:790,335:480);
figure,imshow(cutim,[]);
bin=cutim;
figure, mesh(double(bin));
mat=bin;

dim(1)=length(mat(:,1));
dim(2)=length(mat(1,:));

% Eliminate the saturated points (value 4095)
[maxval,maxidx]=max(bin);
cutpixel=20;
while( max(maxval)==4095 )
  for jj=1:length(maxval)
    if(maxval(jj)==4095)
      if( maxidx(jj)>cutpixel && jj>cutpixel)
        mat(maxidx(jj)-cutpixel:maxidx(jj)+cutpixel,...
          jj-cutpixel:jj+cutpixel)=0;
      end
      if( maxidx(jj)<=cutpixel && jj>cutpixel)
        mat(1:2*cutpixel,jj-cutpixel:jj+cutpixel)=0;
      end
      if( maxidx(jj)<=cutpixel && jj<=cutpixel )
        mat(1:2*cutpixel,1:2*cutpixel)=0;
      end
      if( maxidx(jj)>cutpixel && jj<=cutpixel )
        mat(maxidx(jj)-cutpixel:maxidx(jj)+cutpixel,...
          1:2*cutpixel)=0;
      end
    end
  end
  [maxval,maxidx]=max(mat);
end

mat=mat(1:dim(1),1:dim(2));
figure,mesh(double(mat));

% Find maximums on the image
[maxval,maxidx]=max(mat);
```

```
% Mimimum intensity of the maximum
height=700;
while( max(maxval)>height )
  realmax=-1;
  idx=1;
  jj=1;
  while(jj<=length(maxval))
    kk=jj;
    loop=true;
    if (maxval(jj)>height)
      while(kk<=length(maxval) && loop==true &&...
          maxval(kk)>height)
        if(maxidx(jj)>=maxidx(kk)-3 && maxidx(jj)<=...
            maxidx(kk)+3)
          idxbegin=jj;
          idxend=kk;
        else
          loop=false;
        end
      kk=kk+1;
    end

    [tmp,colt(idx)]=max(maxval(idxbegin:idxend));
    colt(idx)=colt(idx)+idxbegin-1;
    rowt(idx)=maxidx(colt(idx));

    % The maximum has been found, so we can delete
    % the analysed bead
    cut=8;
    if(rowt(idx)+cut<=length(mat(:,1)) && colt(idx)+cut<=...
      length(mat(1,:)) && rowt(idx)-cut>=1 && colt(idx)-...
        cut>=1 )
      mat(rowt(idx)-cut:rowt(idx)+cut,...
      colt(idx)-cut:colt(idx)+cut)=0;
    end
    if(rowt(idx)+cut<=length(mat(:,1)) && colt(idx)+cut>...
      length(mat(1,:)) && rowt(idx)-cut>=1 )
      mat( rowt(idx)-cut:rowt(idx)+cut,...
      length(mat(1,:))-2*cut:length(mat(1,:)) )=0;
    end
    if(rowt(idx)+cut>length(mat(:,1)) && colt(idx)+cut<=...
      length(mat(1,:)) && colt(idx)-cut>=1 )
      mat(length(mat(:,1))-cut:length(mat(:,1)),...
```

```
        colt(idx)-cut:colt(idx)+cut)=0;
      end
      if(rowt(idx)+cut>length(mat(:,1)) && colt(idx)+cut>...
        length(mat(1,:)))
        mat(length(mat(:,1))-2*cut:length(mat(:,1)),...
        length(mat(1,:))-2*cut:length(mat(1,:)))=0;
      end
      if(rowt(idx)-cut<1 && colt(idx)+cut<= ...
        length(mat(1,:)) && colt(idx)-cut>=1 )
        mat(1:2*cut,colt(idx)-cut:colt(idx)+cut)=0;
      end
      if(rowt(idx)+cut<=length(mat(:,1)) && colt(idx)-cut<1 ...
        && rowt(idx)-cut>=1 )
        mat(rowt(idx)-cut:rowt(idx)+cut,1:2*cut)=0;
      end
      if(rowt(idx)-cut<1 && colt(idx)-cut<1)
        mat(1:2*cut,1:2*cut)=0;
      end
      if(rowt(idx)-cut<1 && colt(idx)+cut>length(mat(1,:)))
        mat(1:2*cut,length(mat(1,:))-2*cut:length(mat(1,:)))=0;
      end
      if(rowt(idx)+cut>length(mat(:,1)) && colt(idx)-cut<1)
        mat(length(mat(:,1))-2*cut:length(mat(:,1)),1:2*cut)=0;
      end

      idx=idx+1;
      jj=idxend+1;
      end
    jj=jj+1;
    [maxval,maxidx]=max(mat);
  end
end

% Save the x and y coordinate of the maximums
idx=1;
nt=length(colt);
for jj=1:nt
  if(rowt(jj)<length(bin(:,1))-4 && colt(jj)<...
        length(bin(1,:)) )
      row(idx)=rowt(jj);
      col(idx)=colt(jj);
      idx=idx+1;
  end
```

```
end

n=length(col);

% Find the height and the width of the beads caused
% by the astigmatism
for jj=1:n
  right=0;
  left=0;
  up=0;
  down=0;
  h=bin(row(jj),col(jj));
  h=h-(h-noise)/2;
  if(col(jj)>2 && row(jj)>2 && row(jj)<length(bin(:,1))-2...
      && col(jj)<length(bin(1,:)) )
    tmpr=col(jj);
    tmpl=col(jj);
    tmpu=row(jj);
    tmpd=row(jj);
    stop=false;
    while( max(max(bin(row(jj)-2:row(jj)+2,tmpr+1:tmpr+2...
        )))>h && stop==false)
      right=right+1;
      if(tmpr<length(bin(1,:))-2)
        tmpr=tmpr+1;
      else
        stop=true;
      end
    end
    stop=false;
    while( max(max(bin(row(jj)-2:row(jj)+2,tmpl-2:tmpl-1)...
        ))>h && stop==false)
      left=left+1;
      if(tmpl>1)
        tmpl=tmpl-1;
      else
        stop=true;
      end
    end
    stop=false;
    while( max(max(bin(tmpd+1:tmpd+2,col(jj)-2:col(jj)+2 )...
        ))>h && stop==false)
      down=down+1;
```

```
        if(tmpr<length(bin(:,1)))
          tmpd=tmpd+1;
        else
          stop=true;
        end
      end
      stop=false;

      while(max(max(bin(tmpu-2:tmpu-1,col(jj)-2:col(jj)+2)...
          ))>h && stop==false)
        up=up+1;
        if(tmpu>3)
          tmpu=tmpu-1;
        else
          stop=true;
        end
      end
      lengthrow(jj)=(left+right)*81e-9;
      lengthcol(jj)=(up+down)*81e-9;
  end
end

% Extrapolate the z-coordinate from the fit of the waist
for jj=1:n
  [tmp,idxrow(jj)]=min(abs(lengthrow(jj)-wrowest));
  [tmp,idxcol(jj)]=min(abs(lengthcol(jj)-wcolest));
  z(jj)=x(floor(idxrow(jj)+idxcol(jj)/2));
end

depthz=z;
for jj=1:7
  cutim(row(jj)-6:row(jj)+6,col(jj)-1:col(jj)+6)=0;
  figure,imshow(cutim,[]);
end

% Convert the cooridnate in metre
row=row*81e-9;
col=col*81e-9;

% Plot the beads in the 3D space
for jj=2:n
  [a,b,c] = ellipsoid(row(jj),col(jj),z(jj),110e-9,...
    110e-9,erry);
```

```
    set(gcf,'Color','black')
    set(gca,'Xcolor',[1 1 1]);
    set(gca,'Ycolor',[1 1 1]);
    set(gca,'Zcolor',[1 1 1]);
    mesh(a,b,c),xlabel('y [m]'), ylabel('x [m]'),...
      zlabel('z [m]'),axis([0 max(row)+10e-7 ...
      0 max(col)+10e-7 min(z)-1e-7 max(z)+1e-7]),...
      hold on, set(gca,'Color','k'),...
      title('Z-stack quantum beads');
end
```

Bibliography

[1] S. Bonora, Y. Jian, P. Zhang, A. Zam, E. N. Pugh Jr., R. Zawadzki, M. Sarunic *Wavefront correction and high-resolution in vivo OCT imaging with an objective integrated multi-actuator adaptive lens*, Optics Express 21931, Vol. 23 (No. 17), 2015.

[2] D. Dèbarre, M. J. Booth and T. Wilson, *Image based adaptive optics through optimisation of low spatial frequencies*, Optics Express, Vol. 15 (No. 13), 8176-8190, 2007.

[3] J. R. Fienup, *Phase retrieval algorithms: a comparison*, Applied Optics, Vol. 21 (No. 15), 2758-2769, 1982.

[4] J. R. Fienup, B. J. Thelen, R. G. Paxman, D. A. Carrara, *Comparison of Phase Diversity and Curvature Wavefront Sensing*, Spie, Vol. 3353, 930-940, 1998.

[5] J. W. Hardy, *Adaptive optics for astronomical telescopes*, Oxford Series in Optical and Imaging Sciences, 1999.

[6] R. W. Gerchberg, W. O. Saxton, *A practical algorithm for the determination of phase from image and diffraction plane pictures*, Optik, Vol. 35 (No. 9), 237-246, 1972.

[7] R. A. Gonsalves, *Phase retrieval from modulus data*, J. Opt. Soc. Am., Vol. 66 (No. 9), 961-964, 1976.

[8] R. A. Gonsalves, *Phase retrieval and diversity in adaptive optics*, Optical Engineering, Vol. 21 (No. 5), 829-832, 1982.

[9] R. A. Gonsalves, R. Chidlaw, *Wavefront sensing by phase retrieval*, SPIE, Vol. 207, Applications of Digital Image Processing, 32-39, 1979.

[10] R. A. Muller, A. Buffington, *Real-time correction of atmospherically degraded telescope images through image sharpening*, Journal of the Optical Sociey of America, Vol. 64 (No. 9), 1200-1210, 1974.

[11] Optotune, *http://www.optotune.com/images/products/Optotune%20EL-10-30.pdf.*

[12] R. Ragazzoni, *Pupil plane wavefront sensing with an oscillating prism*, Journal of Modern Physics, Vol. 43 (No. 2), 289-293, 1996.

[13] L. Rizzotto, *Confocal microscopy with sensorless adaptive optics*, Master thesis.

[14] F. Roddier, *Adaptive optics in astronomy*, Cambridge University Press, 1999.

[15] F. Roddier, *Curvature sensing and compensation: a new concept in adaptive optics*, Applied Optics, Vol. 27 (No. 7), 1223-1225, 1988.

[16] C. Roddier, F. Roddier, *Wave-front reconstruction from defocused images of ground-based optical telescopes*, J. Opt. Soc. Am. A, Vol. 10 (No. 11), 2277-2288, 1993.

[17] F. Roddier, C. Roddier, *Wavefront reconstruction using iterative Fourier transforms*, Applied Optics, Vol. 30, 1325-1327, 1991.

[18] M.J. Rust, M. Bates, X. Zhuang *Sub-diffraction-limit imaging by stochastic optical reconstruction microscopy (STORM)*, Nature Methods, Vol. 3 (No. 10), 793-795, 2006.

[19] C. Schwartz, E. Ribak, and S. G. Lipson, *Bimorph adaptive mirrors and curvature sensing*, J. Opt. Soc. Am. A, Vol. 11 (No. 2), 895-902, 1994.

[20] E. Steinhaus, S. G. Lipson, *Bimorph piezoelectric flexible mirror*, J. Opt. So. Am, Vol. 69 (No. 3), 478-481, 1979.

[21] M. R. Teague, *Deterministic phase retrieval: a Green's function solution*, J. Opt. So. Am, Vol. 73 (No. 11), 1434-1441, 1983.

[22] Varioptic, *http://www.varioptic.com/technology/electrowetting.*

[23] G. Vdovin, O. Soloviev, A. Samokhin, M. Loktev, *Correction of low order aberrations using continuous deformable mirrors*, Optics Express 2859, Vol. 16 (No. 5), 2008.

[24] B. Wang, M. J. Booth, *Optimum deformable mirror modes for sensorless adaptive optics*, Optics Communication 282, 4467-4474, 2009.

[25] W. Wang, M. Bates, X. Zhuang *Three-dimensional super-resolution imaging by stochastic optical reconstruction microscopy*, Science, Vol. 319, 810-813, 2008.

Acknowledgements

Ringrazio il mio relatore, il Prof. Stefano Bonora, per l'aiuto nel portare a termine questo lavoro e per avermi fatto insistere quando qualcosa non riusciva. Questa esperienza sarà preziosa per il futuro, ne sono grato.

Un grande grazie va a mamma e papà per avermi sempre sostenuto e aiutato nelle mie scelte. Grazie anche a mio fratello Alberto, con te c'è sempre allegria e movimento.
Ringrazio i miei nonni, per i momenti trascorsi insieme, e i miei parenti, in particolare Egidio e Umberto: sarebbe stato bello ci foste anche voi.
Grazie a tutti i miei amici. Alberto, con te chiacchierare e giocare a PES è sempre splendido. Francesco, con te le discussioni di musica e strumentazione sono sempre illuminanti. Con voi due, Marco e Flavio è sempre un piacere suonare.
Ringrazio anche Caterina, Imerio, Giovanni e Maria. Mi avete accolto come facessi parte della famiglia.

Infine ringrazio Anna, il tuo amore non è mai ricambiato abbastanza e il tuo aiuto e supporto sempre fondamentali. Illumini le mie giornate.